inorganics

MDPI

Article

3–(2–Pyridyl)pyrazole Based Luminescent 1D-Coordination Polymers and Polymorphic Complexes of Various Lanthanide Chlorides Including Orange-Emitting Cerium(III)

Heba Youssef [1,2], Alexander E. Sedykh [1], Jonathan Becker [1], Ilya V. Taydakov [3] and Klaus Müller-Buschbaum [1,4,*]

[1] Institute of Inorganic and Analytical Chemistry, Justus–Liebig–University Giessen, Heinrich–Buff–Ring 17, 35392 Giessen, Germany
[2] Department of Chemistry, Faculty of Science, Mansoura University, El Gomhouria, Mansoura Qism 2, Dakahlia Governorate, Mansoura 11432, Egypt
[3] Lebedev Physical Institute of the Russian Academy of Sciences, Leninskiy pr–t, 53, 119991 Moscow, Russia
[4] Center of Materials Research (LAMA), Justus–Liebig–University Giessen, Heinrich–Buff–Ring 16, 35392 Giessen, Germany
* Correspondence: klaus.mueller-buschbaum@anorg.chemie.uni-giessen.de

Abstract: A series of 18 lanthanide-containing 1D-coordination polymers $^{1}{}_{\infty}[Ln_2(2–PyPzH)_4Cl_6]$, Ln = La, Nd, Sm, dinuclear polymorphic complexes α–, β–$[Ln_2(2–PyPzH)_4Cl_6]$, Ln = Sm, Eu, Gd, α–$[Tb_2(2–PyPzH)_4Cl_6]$, and $[Gd_2(2–PyPzH)_3(2–PyPz)Cl_5]$, mononuclear complexes $[Ce(2–PyPzH)_3Cl_3]$, $[Ln(2–PyPzH)_2Cl_3]$, Ln = Tb, Dy, Ho, and Er, and salt-like complexes $[Gd_3(2–PyPzH)_8Cl_8]Cl$ and $[PyH][Tb(2–PyPzH)_2Cl_4]$ were obtained from the reaction of the respective lanthanide chloride with the 3–(2–pyridyl)pyrazole (2–PyPzH) ligand at different temperatures. An antenna effect through ligand-to-metal energy transfer was observed for several products, leading to the highest luminescence efficiency displayed by a quantum yield of 92% in $[Tb(2–PyPzH)_2Cl_3]$. The Ce^{3+} ion in the complex $[Ce(2–PyPzH)_3Cl_3]$ exhibits a bright and orange 5d-based broadband emission with a maximum at around 600 nm, marking an example of a strong reduction of the 5d-excited states of Ce(III). The absorption spectroscopy shows ion-specific 4f–4f transitions, which can be assigned to Nd^{3+}, Sm^{3+}, Eu^{3+}, Dy^{3+}, Ho^{3+}, and Er^{3+} in a wide spectral range from UV–VIS to the NIR region.

Keywords: N-donor ligand; luminescence; polymorphism; cerium; lanthanides

check for updates

Citation: Youssef, H.; Sedykh, A.E.; Becker, J.; Taydakov, I.V.; Müller-Buschbaum, K. 3–(2–Pyridyl)pyrazole Based Luminescent 1D-Coordination Polymers and Polymorphic Complexes of Various Lanthanide Chlorides Including Orange-Emitting Cerium(III). *Inorganics* **2022**, *10*, 254. https://doi.org/10.3390/inorganics10120254

Academic Editor: László Kótai

Received: 11 October 2022
Accepted: 8 December 2022
Published: 10 December 2022

1. Introduction

The coordination polymers (CPs) and complexes of lanthanides with N-donor ligands have been the focus of research efforts in recent decades [1–5]. Their hybrid nature results in distinctive photoluminescence (PL) properties [6–9] alongside a wide variety of other features and properties [10–13]. The PL of the lanthanide ions is mainly based on two types of transitions: 4f–4f or 5d–4f transitions [14]. In general, the emission intensity of 5d–4f transitions is often strong due to their allowed character, resulting in short excited-state lifetimes (<100 ns) [15–19]. The luminescence colors of these lanthanide ions, such as Eu^{2+}, Ce^{3+}, Sm^{2+}, etc., can vary upon the coordination environment due to the influence of the crystal field on the outermost 5d electron shell [20–23]. In contrast, spin-forbidden 4f–4f transitions (lifetimes up to the ms range) [24] with intrinsically low absorption coefficients have the 4f electron shell regularly shielded by the 5d electron shell, and the characteristic emission of these ions are therefore almost independent of the chemical surrounding, as observed in Tb^{3+}, Eu^{3+}, Dy^{3+}, Ho^{3+}, etc., [25]. A key factor is a proper ligand selection to sensitize the Ln^{3+} ion by ligand-to-metal energy transfer [26]. The organic ligand should also possess appropriate energy-donating states for efficient energy transfer [27].

Recently, the investigation and determination of the luminescence properties of Ce^{3+}-based CPs and complexes have increasingly become the focus of scientific interest after several reports in the literature of non-emissive Ce^{3+}-based compounds due to luminescence quenching by linkers and/or solvent molecules [28]. The reported Ce^{3+}-centered luminescence is mainly in the near UV and blue region [22,29,30]. Recently, the green/yellow [31–34] or even the unusual yellow emission [35] of some Ce^{3+}-based doped materials as well as the red emission of Ce/Pr systems and their application in solid-state LEDs have been reported [36–40].

Since 3–(3–pyridyl)pyrazole (3–PyPzH) and 3–(4–pyridyl)pyrazole (4–PyPzH) ligands have recently been used to obtain homoleptic and highly luminescent trivalent lanthanide 3D-CPs with the formula $^{3}_{\infty}$[Ln(3–PyPz)$_3$] and $^{3}_{\infty}$[Ln(4–PyPz)$_3$], Ln = Sm, Eu, Gd, Tb, Dy [7]. In addition, 3–PyPzH has been further used to obtain a variety of 3D-frameworks and 2D-networks as well as complexes of Ln-trichlorides differing in constitution and structure: $^{3}_{\infty}$[Ln(3–PyPzH)Cl$_3$], Ln = Eu, Gd, $^{2}_{\infty}$[Sm(3–PyPzH)Cl$_3$], $^{2}_{\infty}$[Tb$_2$(3–PyPzH)$_3$Cl$_6$]·2Tol, $^{2}_{\infty}$[Ln$_2$(3–PyPzH)$_3$Cl$_6$]·2MeCN, Ln = Eu^{3+}, Tb^{3+}, Dy^{3+}, Ho^{3+}, Er^{3+}, $^{2}_{\infty}$[Ln(3–PyPzH$_2$)Cl$_4$], Ln = La, Nd, and [(3–PyPzH$_2$)][Ln(3–PyPzH)$_2$Cl$_4$], Ln = Eu, Tb, Dy, Ho [2]. An antenna effect through ligand-to-metal energy transfer was observed for several products for both ligands, resulting in the highest luminescence efficiency for Tb^{3+}-based compounds, indicated by quantum yield reaching 76%. The reported results indicate the value of exploring new N-donor-based ligands and coordination compounds to achieve a wide variety of structures and PL for the lanthanides. Consequently, the objective of our work was the synthesis of new CPs and complexes along the lanthanide series with the tridentate ligand 3–(2–pyridyl)pyrazole (2–PyPzH) to develop a better understanding of the photophysical and thermal properties observed for the Ln series, as well as investigating the polymorphism, the ability of a pure compound to adopt more than one packing arrangement in the solid-state [41,42], of the studied compounds.

The highlight of this work is the strong bathochromic shift of the Ce^{3+}-based emission towards the red region of the visible spectrum and the high luminescence efficiency for the Tb^{3+} complex, reaching 92%.

2. Results and Discussion

2.1. Synthesis and Structural Analysis

Solvothermal syntheses of 3–(2–pyridyl)pyrazole (2–PyPzH) with anhydrous lanthanide trichlorides in either acetonitrile (MeCN), toluene (Tol), or pyridine (Py) were implemented to obtain a family of 18 CPs and complexes as shown in Scheme 1.

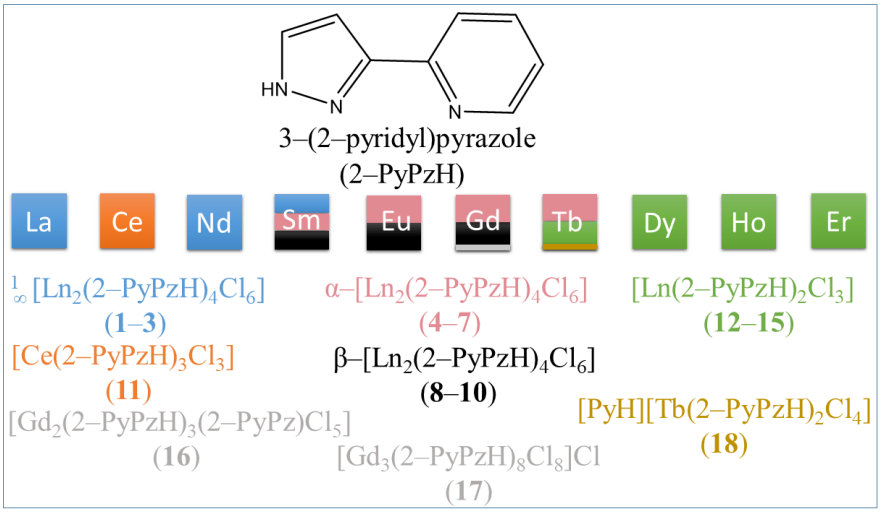

Scheme 1. Structural diversity and polymorphism of the products from the reactions of respective anhydrous $LnCl_3$ with 2–PyPzH. The color changes indicate a different crystal structure.

The structures of $^1{}_\infty[Ln_2(2–PyPzH)_4Cl_6]$, Ln = La (**1**), Nd (**2**), Sm (**3**), α–$[Ln_2(2–PyPzH)_4Cl_6]$, Ln = Eu (**5**), Gd (**6**), Tb (**7**), β–$[Ln_2(2–PyPzH)_4Cl_6]$, Ln = Sm (**8**), Eu (**9**), Gd (**10**), $[Ce(2–PyPzH)_3Cl_3]$ (**11**), $[Ln(2–PyPzH)_2Cl_3]$, Ln = Tb (**12**), Dy (**13**), Ho (**14**), Er (**15**), $[Gd_2(2–PyPzH)_3(2–PyPz)Cl_5]$ (**16**), $[Gd_3(2–PyPzH)_8Cl_8]Cl$ (**17**), and $[PyH][Tb(2–PyPzH)_2Cl_4]$ (**18**) were determined by single crystal X-ray diffraction (SCXRD), whereas the structure of α–$[Sm_2(2–PyPzH)_4Cl_6]$ (**4**) was identified from microcrystalline product by powder X-ray diffraction (PXRD).

$^1{}_\infty[Ln_2(2–PyPzH)_4Cl_6]$, Ln = La (**1**), Nd (**2**), Sm (**3**), α–$[Ln_2(2–PyPzH)_4Cl_6]$, Ln = Sm (**4**), Eu (**5**), Gd (**6**), Tb (**7**), and $[Ln(2–PyPzH)_2Cl_3]$, Ln = Tb (**12**), Dy (**13**), Ho (**14**), Er (**15**) crystallize in the monoclinic crystal system with the space group $C2/c$ for **1**–**3** and $P2_1/c$ for **4**–**7** and **12**–**15**. $[Ce(2–PyPzH)_3Cl_3]$ (**11**) crystallizes in the orthorhombic crystal system of higher symmetry with the space group *Pbca*, while the β–$[Ln_2(2–PyPzH)_4Cl_6]$, Ln = Sm (**8**), Eu (**9**), and Gd (**10**) crystallizes in the triclinic crystal system with the space group $P\bar{1}$.

In $^1{}_\infty[Ln_2(2–PyPzH)_4Cl_6]$ (**1**–**3**), α–$[Ln_2(2–PyPzH)_4Cl_6]$ (**4**–**7**), and β–$[Ln_2(2–PyPzH)_4Cl_6]$ (**8**–**10**), each Ln^{3+} ion coordinates to four Cl^- ligands and four nitrogen atoms in a distorted triangular dodecahedral geometry. In **1**–**3**, a chlorine atom acts as a bridge between two adjacent Ln^{3+} ions to form a 1D-coordination polymer (Figure 1), while two chlorine atoms bridge the two Ln^{3+} ions in the dimeric complexes **4**–**10** (Figures 2 and S1). For the monomer complexes, the Ce^{3+} in $[Ce(2–PyPzH)_3Cl_3]$ (**11**) has a CN of nine coordinated by three chlorides and six nitrogen atoms of three 2–PyPzH ligands in a distorted tricapped trigonal prismatic geometry (Figure 3), while the Ln^{3+} in $[Ln(2–PyPzH)_2Cl_3]$ (**12**–**15**) has a CN of seven and is coordinated by three chloride ions and four nitrogen atoms of two 2–PyPzH ligands in a distorted capped trigonal prism (Figure 4). The differences in the orientation and position of the atoms between the polymorphs α–$[Ln_2(2–PyPzH)_4Cl_6]$ (**5**, **6**) and β–$[Ln_2(2–PyPzH)_4Cl_6]$ (**9**, **10**) are minor when the two structures are overlaid (Figure S2). The α phase (higher crystallographic symmetry) is about 1.2% more densely packed than the β phase, resulting in a slightly shorter metal–metal distance (443.3(1) in **5** and 447.6(1) pm in **9**).

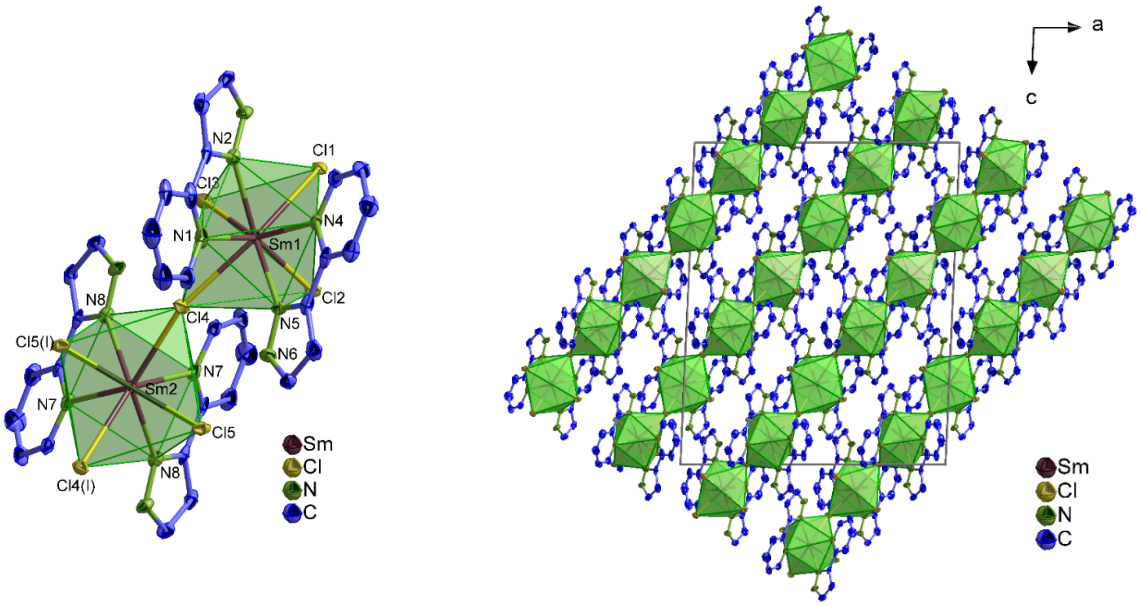

(**a**) (**b**)

Figure 1. (**a**) Extended coordination sphere of the Sm^{3+} ion in $^1{}_\infty[Sm_2(2–PyPzH)_4Cl_6]$ (**3**) representing the isotypic compounds **1**–**3**.; (**b**) crystal structure of **3** with a view along [010]. Symmetry operation: I −x+1,y,−z+1/2. In all figures, the hydrogen atoms are omitted for clarity and the coordination polyhedra around Ln^{3+} are shown in green, with thermal ellipsoids shown with a probability of 50%.

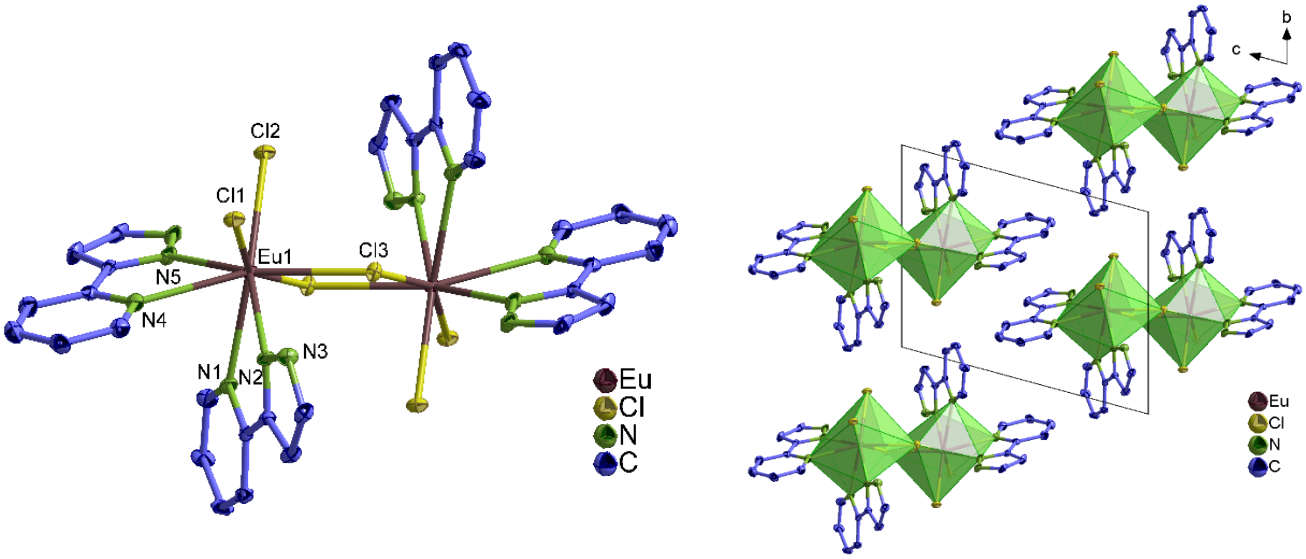

(**a**) (**b**)

Figure 2. (**a**) Extended coordination sphere of the Eu^{3+} ion in β–[Eu_2(2–PyPzH)$_4Cl_6$] (**9**) representing the isotypic compounds **8**–**10**.; (**b**) crystal structure of **9** with a view along [100].

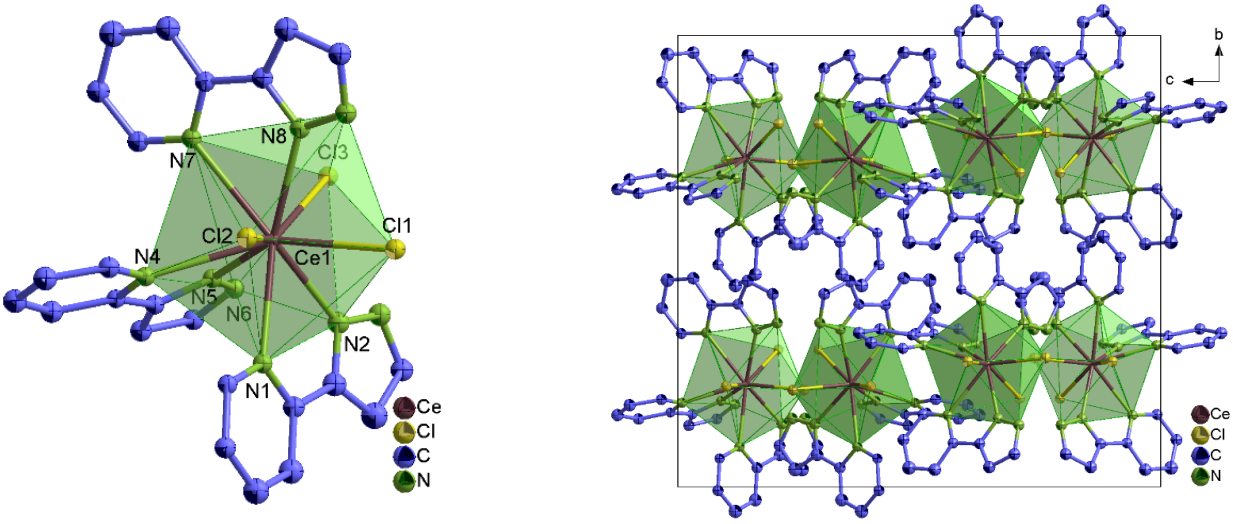

(**a**) (**b**)

Figure 3. (**a**) Extended coordination sphere of the Ce^{3+} ion in [Ce(2–PyPzH)$_3Cl_3$] (**11**).; (**b**) crystal structure of **11** with a view along [100].

The Ln–N and Ln–Cl distances of the studied compounds agree with the expected range for the trivalent Ln ions in halides [43,44]. A comparison of the interatomic distances of β–[Sm_2(2–PyPzH)$_4Cl_6$] (**9**) (average Sm–N 258.3 and Sm–Cl 269.2(1)–277.6(1) pm) with the structurally related complex [Sm(μ–Cl)$_2$Cl$_4$(phen)$_4$]·2CH_3OH, (phen = 1,10–phenanthroline, average Sm–N 258.4 and Sm–Cl 269.1–281.8 pm) [45] resulted in a good agreement for both distances.

A further comparison of [Ce(2–PyPzH)$_3Cl_3$] (**11**) (average Ce–N 270.2 and Ce–Cl 279.7(2)–283.2(1) pm) with the [CeL]Cl_3·4H_2O, (L = a chiral macrocyclic ligand derived from (1*R*,2*R*)–1,2–diphenylethylenediamine and 2,6–diformylpyridine, average Ce–N 273.42 and Ce–Cl 280.0–285.5 pm) [46] resulted in a good agreement for both distances. A further comparison of [Tb(2–PyPzH)$_2Cl_3$] (**12**) (Tb–N(py) 255.9(4), 256.7(4), Tb–Cl 262.2(2) –267.3(2) pm) with the [Ln_2Cl_6(μ–4,4′–bipy)(py)$_6$], (bipy = 4,4′–bipyridine, py = pyridine, Tb–N 254.0–259.3, Tb–Cl 261.68–266.44 pm) [47] shows as well a good agreement for both distances.

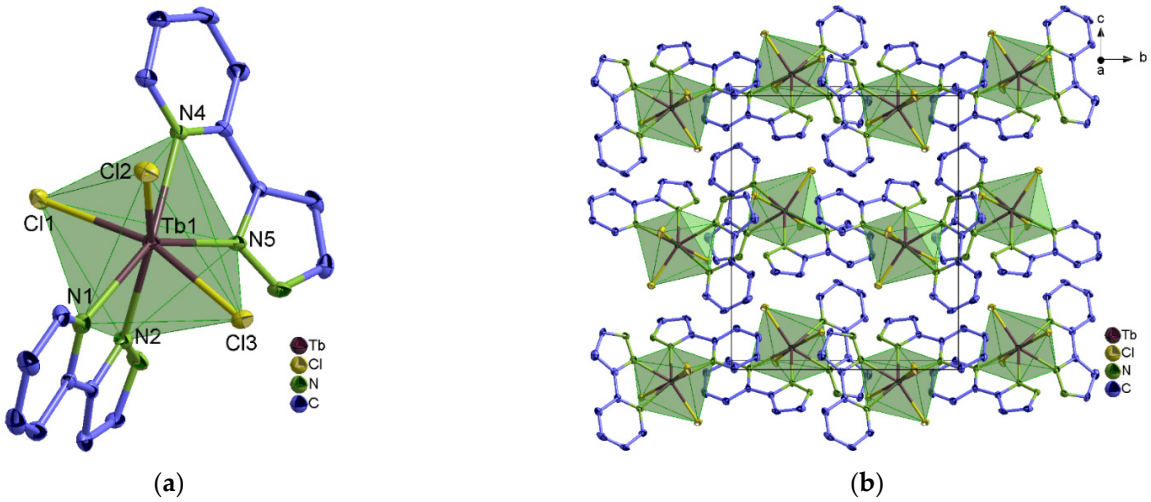

(**a**) (**b**)

Figure 4. (**a**) Extended coordination sphere of the Tb^{3+} ion in $[Tb(2–PyPzH)_2Cl_3]$ (**12**) representing the isotypic complexes **12**–**15**.; (**b**) packing structure of **12** with a view along [100].

Another three complexes of the formula, $[Gd_2(2–PyPzH)_3(2–PyPz)Cl_5]$ (**16**), $[Gd_3(2–PyPzH)_8Cl_8]Cl$ (**17**), and $[PyH][Tb(2–PyPzH)_2Cl_4]$ (**18**), are formed as byproducts and crystallize in the monoclinic, triclinic, and orthorhombic crystal systems with the space groups $P2_1/n$, $P\bar{1}$, and $Pbcn$, respectively. In $[Gd_2(2–PyPzH)_3(2–PyPz)Cl_5]$ (**16**) (Figure S3), both Gd^{3+} are octa-coordinated; one is coordinated to four chlorides and four nitrogen atoms of a 2–PyPzH and a deprotonated $2–PyPz^-$ in a distorted bicapped trigonal prism environment. Two chlorine atoms along with the $2–PyPz^-$ act as a bridge to the second Gd^{3+} ion, which coordinates to another four nitrogen atoms of two 2–PyPzH and a chloride ion in a distorted triangular dodecahedron. For the anionic complex $[Gd_3(2–PyPzH)_8Cl_8]Cl$ (**17**) (Figure S4), all three Gd^{3+} ions are octa-coordinated, forming distorted triangular dodecahedral polyhedra, with two Gd^{3+} ions coordinated to two Cl^- ligands and six nitrogen atoms of three 2–PyPzH. The third Gd^{3+} ion coordinates to four chloride ions and four nitrogen atoms of two 2–PyPzH. Electroneutrality is established by the existence of an uncoordinated chloride ion. For $[PyH][Tb(2–PyPzH)_2Cl_4]$ (**18**) (Figure S5), another distorted triangular dodecahedral polyhedron is formed due to the coordination of the Tb^{3+} ion to four Cl^- ligands and four nitrogen atoms of two 2–PyPzH. Electroneutrality is achieved through the formation of protonated pyridine.

The obtained bulk of the 1D-CPs (**1**–**3**) and the complexes (**4**–**6**, **8**, **9**, **11**–**15**) were investigated by PXRD. The experimental diffraction patterns of the studied compounds agree well with the corresponding diffraction patterns simulated from single crystal data in terms of reflection positions and intensities (Figures 5 and S6–S9). Additional Pawley refinements for **8** and **11** were carried out, confirming the phase purity of the investigated compounds (Figure S10). $\beta–[Gd_2(2–PyPzH)_4Cl_6]$ (**10**) is formed at higher temperatures in a mixture together with the $\alpha–Gd^{3+}$ phase (**6**) (Figure S11). Isolation of $\alpha–[Tb_2(2–PyPzH)_4Cl_6]$ (**7**), $[Gd_2(2–PyPzH)_3(2–PyPz)Cl_5]$ (**16**), $[Gd_3(2–PyPzH)_8Cl_8]Cl$ (**17**), and $[PyH][Tb(2–PyPzH)_2Cl_4]$ (**18**) as single crystals was also possible. Tables with detailed crystallographic data and selected interatomic distances (pm) and angles (○) of the studied compounds are given in the Supplementary Materials (Tables S1–S13).

2.2. Photophysical Properties

2.2.1. UV–VIS–NIR Absorption Spectra

Electronic absorption spectra were recorded in the solid state at room temperature (RT) along with emission and excitation spectra to allow for detailed spectroscopic interpretations for $^1{}_\infty[Ln_2(2–PyPzH)_4Cl_6]$, Ln = La (**1**), Nd (**2**), Sm (**3**), $\alpha–[Ln_2(2–PyPzH)_4Cl_6]$, Ln = Eu (**5**), Gd (**6**), $\beta–[Ln_2(2–PyPzH)_4Cl_6]$, Ln = Sm (**8**), Eu (**9**), $[Ce(2–PyPzH)_3Cl_3]$ (**11**), and $[Ln(2–PyPzH)_2Cl_3]$, Ln = Tb (**12**), Dy (**13**), Ho (**14**), Er (**15**). In the literature, the absorp-

tion spectra have mostly been measured in solution, examining the ligand-based absorption band [48–50], while fewer examples have examined the Ln-based absorption bands in the solid state [2,51–54].

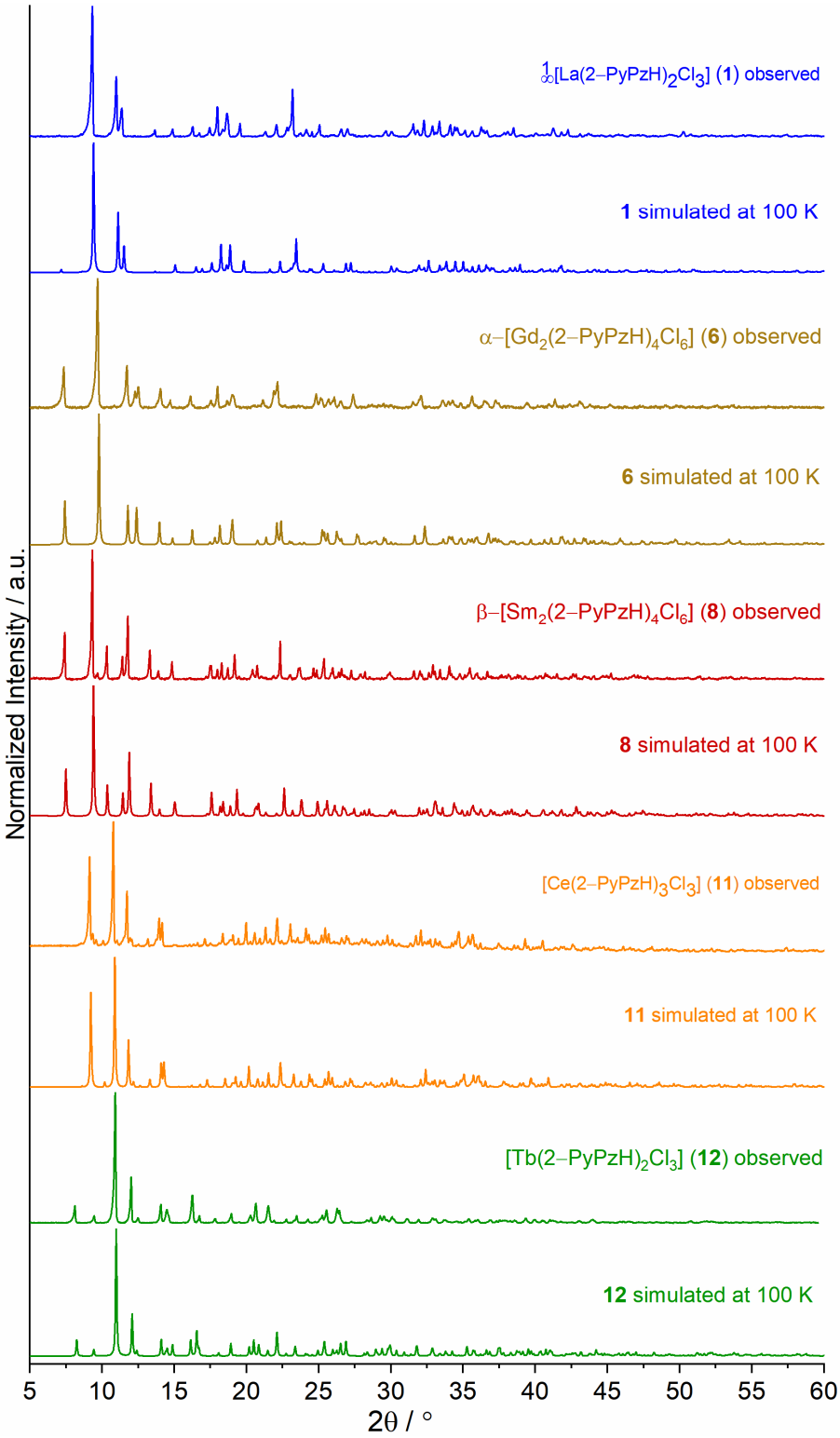

Figure 5. Comparison of exemplary experimental powder X-ray diffraction patterns of $^1_\infty$[La$_2$(2–PyPzH)$_4$Cl$_6$] (**1**), α–[Gd$_2$(2–PyPzH)$_4$Cl$_6$] (**6**), β–[Sm$_2$(2–PyPzH)$_4$Cl$_6$] (**8**), [Ce(2–PyPzH)$_3$Cl$_3$] (**11**), and [Tb(2–PyPzH)$_2$Cl$_3$] (**12**) as representatives of their isotypic 1D-CPs and complexes with the respective simulated pattern from single crystal X-ray data.

The absorption spectrum for 2–PyPzH (Figure S12) was as reported in the literature for the solid state and in acetonitrile solution (7.8×10^{-5} mol L^{-1}), with two characteristic K-band (*ca.* 210~265 nm) and B-band regions (285~350 nm) observed corresponding to the π–π* transitions [55,56]. An intense broad absorption band of the ligand in the UV range was detected for the compounds obtained (Figure 6). In addition, sharp and weak to medium bands originating from the respective f–f transitions (Table 1) in both the VIS and NIR regions for $^{1}{}_{\infty}$[Ln(2–PyPz)$_3$], Ln = Nd (**2**), Sm (**3**), α–[Eu$_2$(2–PyPzH)$_4$Cl$_6$] (**5**), β–[Ln$_2$(2–PyPzH)$_4$Cl$_6$], Ln = Sm (**8**), Eu (**9**), and [Ln(2–PyPzH)$_2$Cl$_3$], Ln = Dy (**13**), Ho (**14**), Er (**15**) ions [54,57–60] were observed. For [Ce(2–PyPzH)$_3$Cl$_3$] (**11**), the formation of a shoulder is observed at higher wavelengths due to the transition from 4f to 5d.

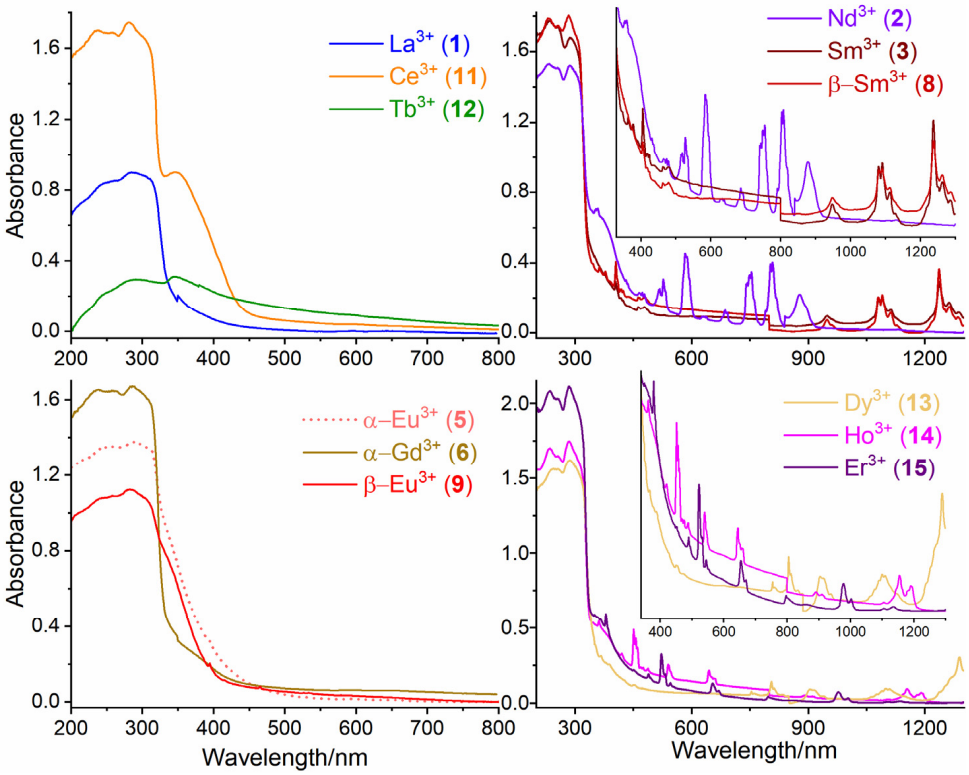

Figure 6. Solid-state absorption spectra of $^{1}{}_{\infty}$[Ln$_2$(2–PyPzH)$_4$Cl$_6$], Ln = La (**1**), Nd (**2**), Sm (**3**), α–[Ln$_2$(2–PyPzH)$_4$Cl$_6$], Ln = Eu (**5**), Gd (**6**), β–[Ln$_2$(2–PyPzH)$_4$Cl$_6$], Ln = Sm (**8**), Eu (**9**), [Ce(2–PyPzH)$_3$Cl$_3$] (**11**), and [Ln(2–PyPzH)$_2$Cl$_3$], Ln = Tb (**12**), Dy (**13**), Ho (**14**), Er (**15**) at room temperature.

2.2.2. Emission and Excitation Spectra

The photoluminescence properties were recorded for all bulk products, $^{1}{}_{\infty}$[Ln$_2$(2–PyPzH)$_4$Cl$_6$], Ln = La (**1**), Nd (**2**), Sm (**3**), α–[Ln$_2$(2–PyPzH)$_4$Cl$_6$], Ln = Sm (**4**), Eu (**5**), Gd (**6**), β–[Ln$_2$(2–PyPzH)$_4$Cl$_6$], Ln = Sm (**8**), Eu (**9**), [Ce(2–PyPzH)$_3$Cl$_3$] (**11**), and [Ln(2–PyPzH)$_2$Cl$_3$], Ln = Tb (**12**), Dy (**13**), Ho (**14**), Er (**15**) in the solid state at RT and 77 K. The complex [Ce(2–PyPzH)$_3$Cl$_3$] (**11**) shows remarkable photoluminescence properties with Ce^{3+}-centered light emission in the orange range of the visible spectrum, which can already be distinguishable by the eye under the UV lamp. The Ce^{3+} orange emitter is an exception within other Ce^{3+}-based emitters. Determinations via photoluminescence spectroscopy (Figure 7) revealed a broadband emission starting at 460 nm with a center at around 600 nm at 77 K and RT, indicating large crystal field splitting and a bathochromic shift for the emission wavelength. The excitation spectrum exhibits a shoulder at 370 nm, corresponding to the lowest energy levels of the crystal field splitting bands of the 5d-excited state of the Ce^{3+} ion. The maximum excitation band is at 315 nm, correlated with the coordinated 2–PyPzH ligand. To the best of our knowledge, an orange–red emitting undoped cerium compound (**11**) has hardly been reported, only for doped systems such

as $Gd_3Ga_5O_{12}$ doped with both Pr^{3+} and Ce^{3+} [40], $Y_3Al_5O_{12}$:Ce nanophosphor doped with Pr^{3+} [61], and the cerium-doped scandate [62,63]. The nanosecond scale luminescence lifetime (τ) of **11** (2.83 ns) (Table 2) results from the parity-allowed nature of the 5d–4f transition. In contrast, the longer lifetime for the parity-forbidden 4f–4f transitions in [Tb(2–PyPzH)$_2$Cl$_3$] (**12**) reaches 1.230(1) ms. By comparing both the lifetime and the quantum yield (QY) measured for Tb^{3+} (**12**) (τ = 1.230 (1) ms, QY = 91.8(1.6)%) with the reported $^3{}_\infty$[Tb(3–PyPz)$_3$], (3–PyPz$^-$ = 3–(3–pyridyl)pyrazolate, τ = 1.0874 ms, QY = 74%), $^3{}_\infty$[Tb(4–PyPz)$_3$] (4–PyPz$^-$ = 3–(4–pyridyl)pyrazolate, τ = 0.6273 ms, QY = 23.2%) [7], $^2{}_\infty$[Tb$_2$(3–PyPzH)$_3$Cl$_6$]·2Tol (3–PyPzH = 3–(3–pyridyl)pyrazole, τ = 2.039 ms, QY = 73.1), $^2{}_\infty$[Tb$_2$(3–PyPzH)$_3$Cl$_6$]·2MeCN, (τ = 2.294 ms, QY = 76%) [2], [Tb(bbpen)Cl] (bbpen^{2-} = N,N′–bis(2–oxidobenzyl)–N,N′–bis(pyridin–2–ylmethyl)–ethylenediamine, τ = 0.814 ms, QY = 90%), and [Ln(bbppn)Cl] (bbppn^{2-} = N,N′–bis(2–oxidobenzyl)–N,N′–bis–(pyridin–2–ylmethyl)–1,2–propanediamine, τ = 0.969 ms, QY = 92%) [64], the complex [Tb(2–PyPzH)$_2$Cl$_3$] (**12**) reaches the highest QYs reported among the related Tb-based compounds. The value of τ and QY for the Eu^{3+} containing α–[Eu$_2$(2–PyPzH)$_4$Cl$_6$] (**5**, τ = 1.15(1) ms, QY = 7.6(2)%), β–[Eu$_2$(2–PyPzH)$_4$Cl$_6$] (**9**, τ = 1.19(2) ms, QY = 12.8(6)%), and Dy^{3+} containing [Dy(2–PyPzH)$_2$Cl$_3$] (**13**, τ = 17.14(3) µs, QY = 3.3%) are also higher than for $^3{}_\infty$[Eu(3–PyPz)$_3$], (τ = 0.576 ms, QY = 0.33%), $^3{}_\infty$[Eu(4–PyPz)$_3$], (τ = 0.323 ms, QY = 0.11%), $^3{}_\infty$[Eu(3–PyPzH)Cl$_3$] (τ = 0.2201 ms, QY = <0.5%), $^2{}_\infty$[Eu$_2$(3–PyPzH)$_3$Cl$_6$]·2MeCN (τ = 0.170 ms, QY = na), $^3{}_\infty$[Dy(3–PyPz)$_3$] (τ = 15 µs, QY = 1.13%), and $^3{}_\infty$[Dy(4–PyPz)$_3$] (τ = 12.07 µs, QY = 1.15%). These values decrease significantly for Sm^{3+} (**3**), α–Sm^{3+} (**4**), and β–Sm^{3+} (**8**), reflecting an excellent antenna effect for Tb^{3+} (**12**), where the ligand is mainly responsible for the excitation and a good antenna effect for α–Eu^{3+} (**5**), β–Eu^{3+} (**9**), and Dy^{3+} (**13**), where additional weak direct 4f–4f excitation is present, indicated by a series of ion-specific sharp lines of low intensity and more distinguishable in Nd^{3+} (**2**), Sm^{3+} (**3**), α–Sm^{3+} (**4**), β–Sm^{3+} (**8**), and Er^{3+} (**15**) (Figures 7 and 8).

Table 1. Absorption wavelengths of the transitions of $^1{}_\infty$[Ln$_2$(2–PyPzH)$_4$Cl$_6$], Ln = Nd (**2**), Sm (**3**), α–[Eu$_2$(2–PyPzH)$_4$Cl$_6$] (**5**), β–[Ln$_2$(2–PyPzH)$_4$Cl$_6$], Ln = Sm (**8**), Eu (**9**), and [Ln(2–PyPzH)$_2$Cl$_3$], Ln = Dy (**13**), Ho (**14**), Er (**15**) in the solid state at room temperature.

Intra–4f Absorption Transitions			λ_{max} (nm)
Nd^{3+} (**2**)	$^4I_{9/2}\rightarrow$	$^4D_{3/2}$, $^2P_{1/2}$, $(^2D, ^2P)_{3/2}$, $^4G_{7/2}/^2K_{13/2}$, $^4G_{5/2}$, $^2H_{11/2}$, $^4F_{9/2}$, $^4F_{7/2}$, $^4F_{5/2}$, $^4F_{3/2}$	359, 431, 473, 527, 583, 633, 686, 745, 807, 878 nm
Sm^{3+} (**3**)	$^6H_{5/2}\rightarrow$	$^4F_{7/2}/^6P_{3/2}/^4K_{11/2}$, $(^6P,^4P)_{5/2}$, $^4M_{19/2}$, $^4I_{13/2}$, $^4I_{11/2}$, $^4G_{7/2}$, $^4F_{3/2}$, $^4G_{5/2}$, $^6F_{11/2}$, $^6F_{9/2}$, $^6F_{7/2}$	405, 417, 425, 462, 479, 501, 529, 562, 948, 1090, 1237 nm
α–Eu^{3+} (**5**)	$^7F_0\rightarrow$	$^5L_6$, $^5D_2$, $^5D_1$, $^5D_0$	394, 465, 534, 579 nm
β–Sm^{3+} (**8**)	$^6H_{5/2}\rightarrow$	$^4H_{9/2}/^4D_{7/2}$, $^5D_{5/2}$, $^6P_{7/2}$, $^4F_{7/2}/^6P_{3/2}/^4K_{11/2}$, $(^6P,^4P)_{5/2}$, $^4M_{19/2}$, $^4I_{13/2}$, $^4I_{11/2}$, $^4G_{7/2}$, $^4F_{3/2}$, $^4G_{5/2}$, $^6F_{11/2}$, $^6F_{9/2}$, $^6F_{7/2}$	346, 363, 378, 405, 418, 424, 462, 478, 501, 529, 562, 947, 1083, 1240 nm
β–Eu^{3+} (**9**)	$^7F_0\rightarrow$	$^5L_6$, $^5D_3$, $^5D_2$, $^5D_1$, $^5D_0$	395, 415, 465, 534, 579 nm
Dy^{3+} (**13**)	$^6H_{15/2}\rightarrow$	$^5P_{5/2}$, $^4M_{21/2}/^4K_{17/2}$, $^4G_{11/2}$, $^4I_{15/2}$, $^4F_{9/2}$, $^6F_{3/2}$, $^6F_{5/2}$, $^6F_{7/2}$, $^6F_{9/2}$, $^6F_{11/2}$	366, 387, 427, 450, 474, 754, 805, 903, 1100, 1289 nm
Ho^{3+} (**14**)	$^7I_8\rightarrow$	$(^5G,^3H)_5/^3H_6$, $(^5G,^3G)_5$ $^5G_6$, $^5F_2$, $^5F_3$, $^5F_4$, $^5F_5$, $^5I_5$, $^5I_6$	362, 420, 451, 475, 488, 540, 645, 891, 1154 nm
Er^{3+} (**15**)	$^4I_{15/2}\rightarrow$	$^4G_{11/2}$, $^5F_{5/2}$, $^4F_{7/2}$, $^2H_{11/2}$, $^4S_{8/2}$, $^4F_{9/2}$, $^4I_{11/2}$	379, 452, 489, 522, 545, 654, 978 nm

A broad emission band was visible in the region from about 400–600 nm at 77 K in $^1{}_\infty$[La$_2$(2–PyPzH)$_4$Cl$_6$] (**1**) and α–[Gd$_2$(2–PyPzH)$_4$Cl$_6$] (**6**) and characterized to the triplet state of 2–PyPzH with λ_{onset} = 425 nm (23,529 cm^{-1}). The energy differences (ΔE) between the organic ligand triplet state and the energy position of Tb^{3+} ($^5D_4$ = 20,500 cm^{-1}) [57,59] considering the Latva's rule, ΔE = 3029 cm^{-1}, explain the long lifetime and the excellent quantum yield value of Tb^{3+}.

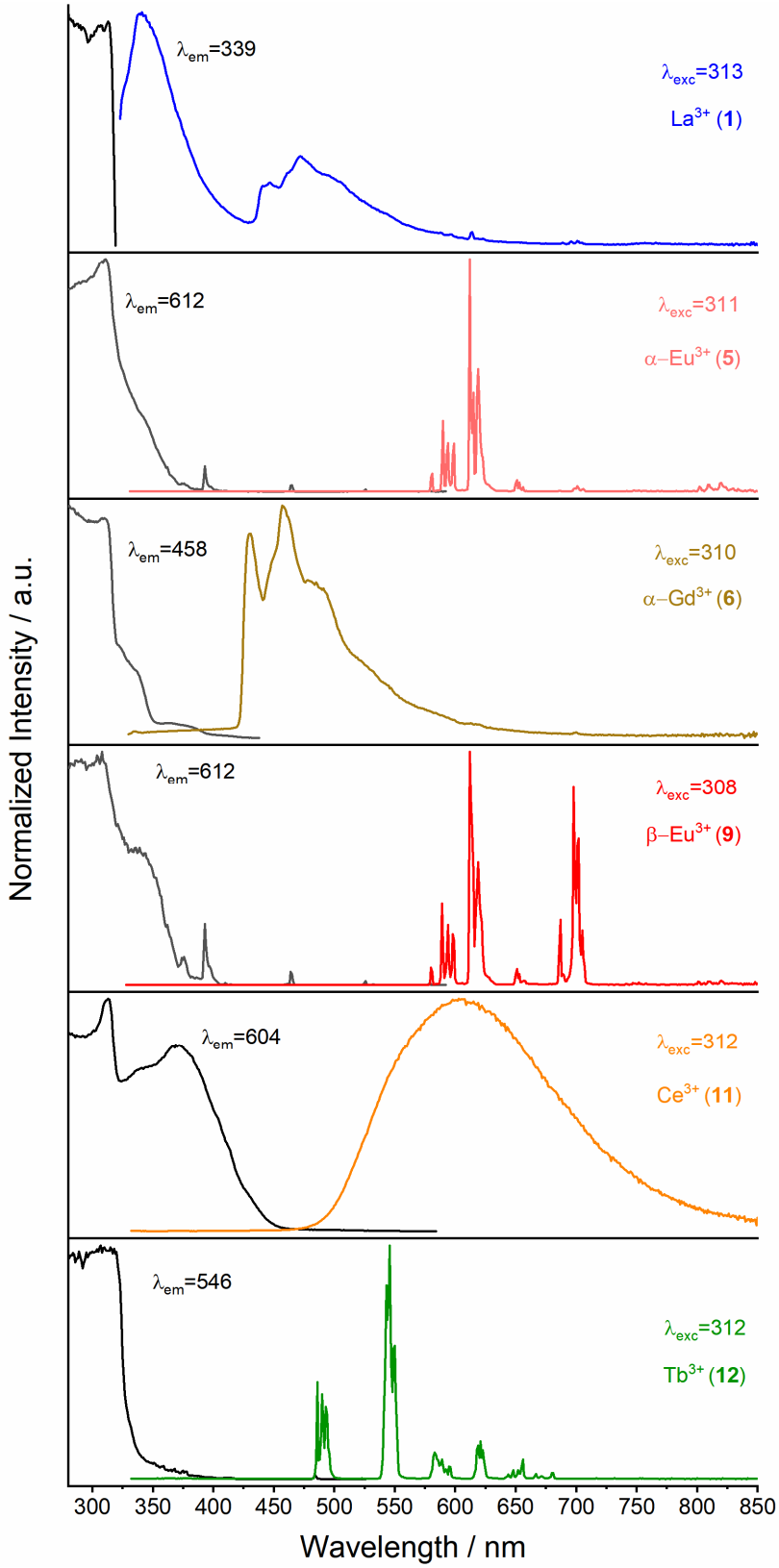

Figure 7. Normalized solid-state excitation (black) and emission spectra (colored) of $^{1}{}_{\infty}[La_2(2\text{–}PyPzH)_4Cl_6]$ (**1**), α–$[Ln_2(2\text{–}PyPzH)_4Cl_6]$, Ln = Eu (**5**), Gd (**6**), β–$[Eu_2(2\text{–}PyPzH)_4Cl_6$ (**9**), $[Ce(2\text{–}PyPzH)_3Cl_3]$ (**11**), and $[Tb(2\text{–}PyPzH)_2Cl_3]$ (**12**) at 77 K. Wavelengths for which the spectra were recorded are given in the legends.

Table 2. Photophysical data of $^{1}{}_{\infty}[Ln_2(2–PyPzH)_4Cl_6]$, Ln = La (**1**), Sm (**3**), α–$[Ln_2(2–PyPzH)_4Cl_6]$, Ln = Sm (**4**), Eu (**5**), Gd (**6**), β–$[Ln_2(2–PyPzH)_4Cl_6]$, Ln = Sm (**8**), Eu (**9**), $[Ce(2–PyPzH)_3Cl_3]$ (**11**), and $[Ln(2–PyPzH)_2Cl_3]$, Ln = Tb (**12**), Dy (**13**) in the solid state at RT and 77 K.

ID	$\tau_{(RT)}$ [1]	$\lambda_{ex}/\lambda_{em}$ [nm] [2]	$\tau_{(77\ K)}$ [3]	$\lambda_{ex}/\lambda_{em}$ [nm] [4]	Φ [%] [5]	$\lambda_{ex}/\lambda_{em}$ [nm] [6]
La^{3+} (**1**)	1.89(3) ns	287/364	1.41(1) ns	287/339	n/a	n/a
Sm^{3+} (**3**)	4.02(9) µs	321/598	1.23(3) ns	287/605	n/a	n/a
α–Sm^{3+} (**4**)	1.17(2) ns	287/599	1.09(2) ns	287/599	n/a	n/a
α–Eu^{3+} (**5**)	1.15(1) ms	305/612	1.435(3) ms	311/612	7.6(2)	310/570–720
α–Gd^{3+} (**6**)	0.117(2) ms	289/545	1.034(4) ms	310/458	n/a	n/a
β–Sm^{3+} (**8**)	2.7(1) µs	316/599	20.7(5) µs	316/599	n/a	n/a
β–Eu^{3+} (**9**)	1.19(2) ms	311/612	1.556(4) ms	308/612	12.8(6)	310/575–715
Ce^{3+} (**11**)	2.83(3) ns	368/595	5.6(1) ns	368/604	n/a	n/a
Tb^{3+} (**12**)	1.230(1) ms	321/546	1.287(1) ms	321/546	91.8(1.6)	318/473–692
Dy^{3+} (**13**)	17.14(3) µs	321/573	13.19(1) µs	321/574	3.3(1)	320/459–763

[1] Emission lifetimes determined at RT. [2] Excitation and emission wavelengths for the emission lifetime at RT. [3] Emission lifetime determined at 77 K. [4] Excitation and emission wavelengths for the emission lifetime at 77 K. [5] Quantum yield. [6] Excitation wavelength and emission range of QY determinations.

For $[Tb(2–PyPzH)_2Cl_3]$ (**12**), α–$[Eu_2(2–PyPzH)_4Cl_6]$ (**5**), and β–$[Eu_2(2–PyPzH)_4Cl_6]$ (**9**) (Figure 7), the highest intensity is found for the transitions $^5D_0 \rightarrow {}^7F_5$ at 545 nm and $^5D_4 \rightarrow {}^7F_2$ at 612 nm as expected for Tb^{3+} and Eu^{3+} ions [65,66], while multiple emission lines are Stark levels as a result of energy-level splitting due to the crystal field.

For α–Eu^{3+} (**5**), the hypersensitive transition $^5D_0 \rightarrow {}^7F_2$ shows a higher number of Stark components (612, 615, and 619 nm) than the triclinic β–Eu^{3+} (**9**) with two Stark components (612, 619 nm) and a higher intensity for the environmentally dependent transition $^5D_0 \rightarrow {}^7F_4$ at 77 K, confirming the different symmetry of the Eu^{3+} centers in **5** and **9**. For the transitions $^5D_0 \rightarrow {}^7F_J$, (J = 1, 3, 4) more Stark splitting is observed for α–Eu^{3+} (**5**) and β–Eu^{3+} (**9**) than the previously reported orthorhombic $^{3}{}_{\infty}[Eu(3–PyPzH)Cl_3]$, confirming the low symmetry for the former. For $^{1}{}_{\infty}[Sm(2–PyPzH)_4Cl_6]$ (**3**), α–$[Sm_2(2–PyPzH)_4Cl_6]$ (**4**), β–$[Sm_2(2–PyPzH)_4Cl_6]$ (**8**), $[Ln(2–PyPzH)_2Cl_3]$, Ln = Dy (**13**), and Ho (**14**) (Figure 8), the highest intensity is found at 600 nm (for Sm^{3+}, corresponds to $^4G_{5/2} \rightarrow {}^6H_{7/2}$), 574 nm (for Dy^{3+}, corresponds to $^4F_{9/2} \rightarrow {}^6H_{13/2}$), and 662 nm (for Ho^{3+}, corresponds to $^5F_5 \rightarrow {}^5I_8$). The f–f transitions are dominant in the 1D-CP of Sm^{3+} (**3**), while the ligand emission is more dominant in the β–Sm^{3+} (**8**) and further overlaps with the f–f transitions in the α–Sm^{3+} (**4**), which has its effect on the lifetime results; τ decreases from **3** (4.02(9) µs) through **8** (2.7(1) µs) to **4** (1.17(2) ns). This behavior reflects the quenching effect arising from the separation of the luminescent metal centers by the extended N-ligands [67], where a Cl^- ligand acts as a bridge between two neighboring Sm^{3+} ions in **3** and two Cl^- ligands act as bridges in **8** and **4**. NIR emission bands can also be observed for **3**, **4**, and **8** at about 790, 900, 945, 1030, and 1175 nm, corresponding to the transitions $^4G_{5/2} \rightarrow {}^6H_{13/2}$ and $^4G_{5/2} \rightarrow {}^6F_{J/2}$, J = 3, 5, 7, 9 of Sm^{3+}, as well as for **13** at 760, 850, 937, 1016, and 1178 nm corresponding to $^4F_{9/2} \rightarrow {}^6H_{J/2}$, (J = 9, 7, 5) and $^6F_{J/2}$, (J = 7, 5) of Dy^{3+} and for **14** at 991 and 1163 nm to $^5F_5 \rightarrow {}^5I_7$ and $^5I_6 \rightarrow {}^5I_8$, respectively.

For $^{1}{}_{\infty}[Nd(2–PyPzH)_4Cl_6]$ (**2**) and $[Er(2–PyPzH)_2Cl_3]$ (**15**), NIR emission bands at 887, 1066, and 1351 nm can also be observed, which correlate with the transitions $^4F_{3/2} \rightarrow {}^4I_{J/2}$, (J = 9, 11, 13) of Nd^{3+}, respectively, and for **15** at 1532 nm, correlated with the transition $^4I_{13/2} \rightarrow {}^4I_{15/2}$ of Er^{3+}. For $^{1}{}_{\infty}[La_2(2–PyPzH)_4Cl_6]$ (**1**), few peaks with very low intensity around 620 and 675 nm are attributed to impurities in the ppm range together with an efficient ligand-to-metal energy transfer. See the Supplementary Materials for half-page size absorption and photoluminescence spectra with designated 4f–4f transitions for the studied compounds (Figures S12–S38).

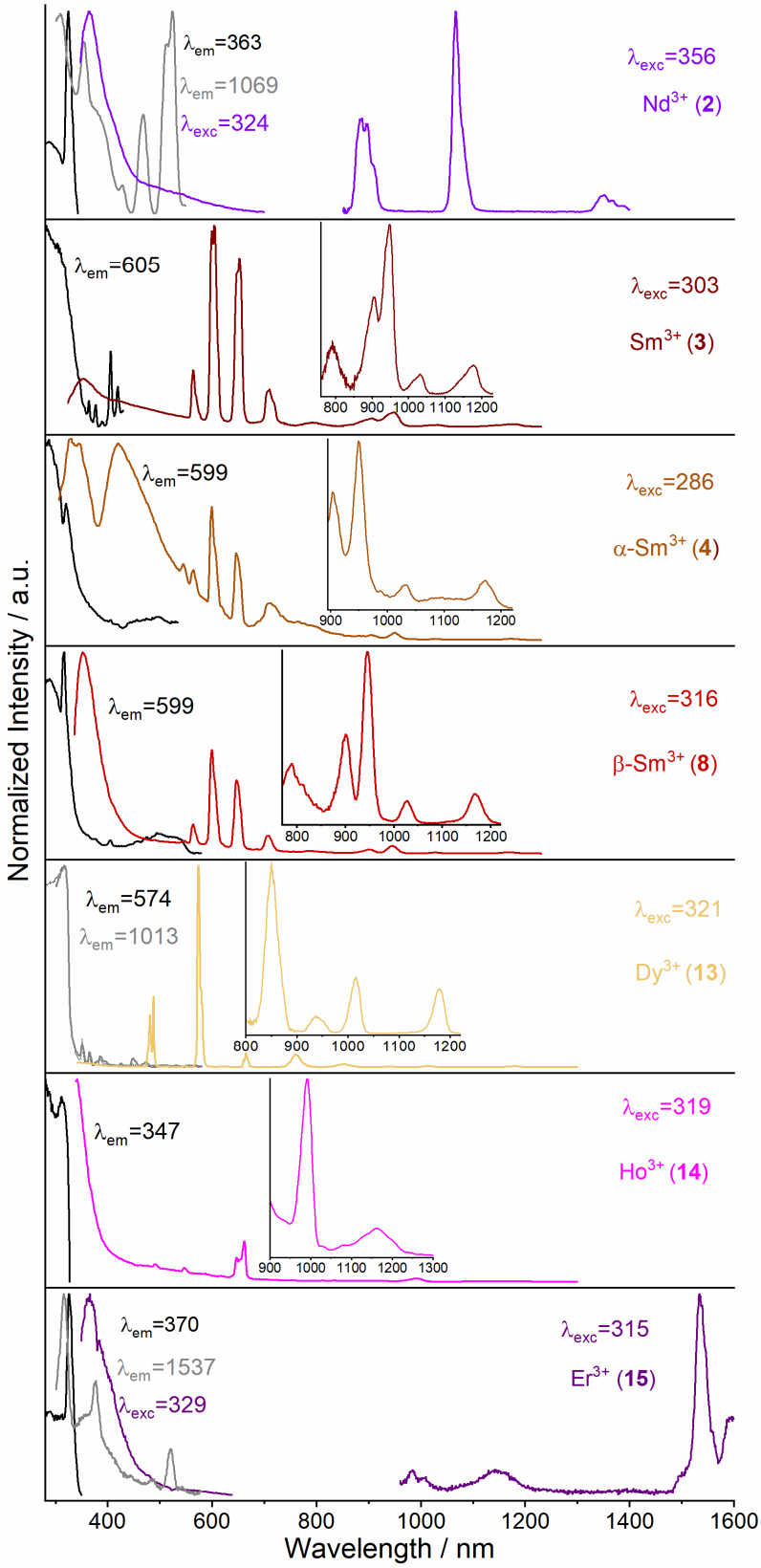

Figure 8. Normalized solid-state excitation (black) and emission spectra (colored) of $^{1}{}_{\infty}[Ln_2(2\text{–}PyPzH)_4Cl_6]$, Ln = Nd (**2**), Sm (**3**), α–$[Sm_2(2\text{–}PyPzH)_4Cl_6]$ (**4**), β–$[Sm_2(2\text{–}PyPzH)_4Cl_6]$ (**8**), and $[Ln(2\text{–}PyPzH)_2Cl_3]$, Ln = Dy (**13**), Ho (**14**), Er (**15**) at 77 K. Wavelengths for which the spectra were recorded are given in the legends.

2.3. Thermal Analysis

Simultaneous DTA and TG studies combined with mass spectrometry were performed for $^{1}{}_{\infty}[Sm_2(2–PyPzH)_4Cl_6]$ (**3**), α–$[Eu_2(2–PyPzH)_4Cl_6]$ (**5**), β–$[Eu_2(2–PyPzH)_4Cl_6]$ (**9**), and $[Tb(2–PyPzH)_2Cl_3]$ (**12**) (Figure 9). For $^{1}{}_{\infty}[Sm_2(2–PyPzH)_4Cl_6]$ (**3**) (Figure 9a), a release of one equivalent of 2–PyPzH (theoretical mass loss = 26.5%) is indicated by the first endothermic signal (signal 1) starting at 250 °C with a mass loss of 26.4%. The second equivalent of 2–PyPzH is not fully released within the following two endothermic signals (2, 3) with a mass loss of 18.1%. A further mass loss is observed at higher temperatures, coinciding with the decomposition of the remaining 2–PyPzH, with black residues observed after the measurement, indicating partial carbonization of the ligand.

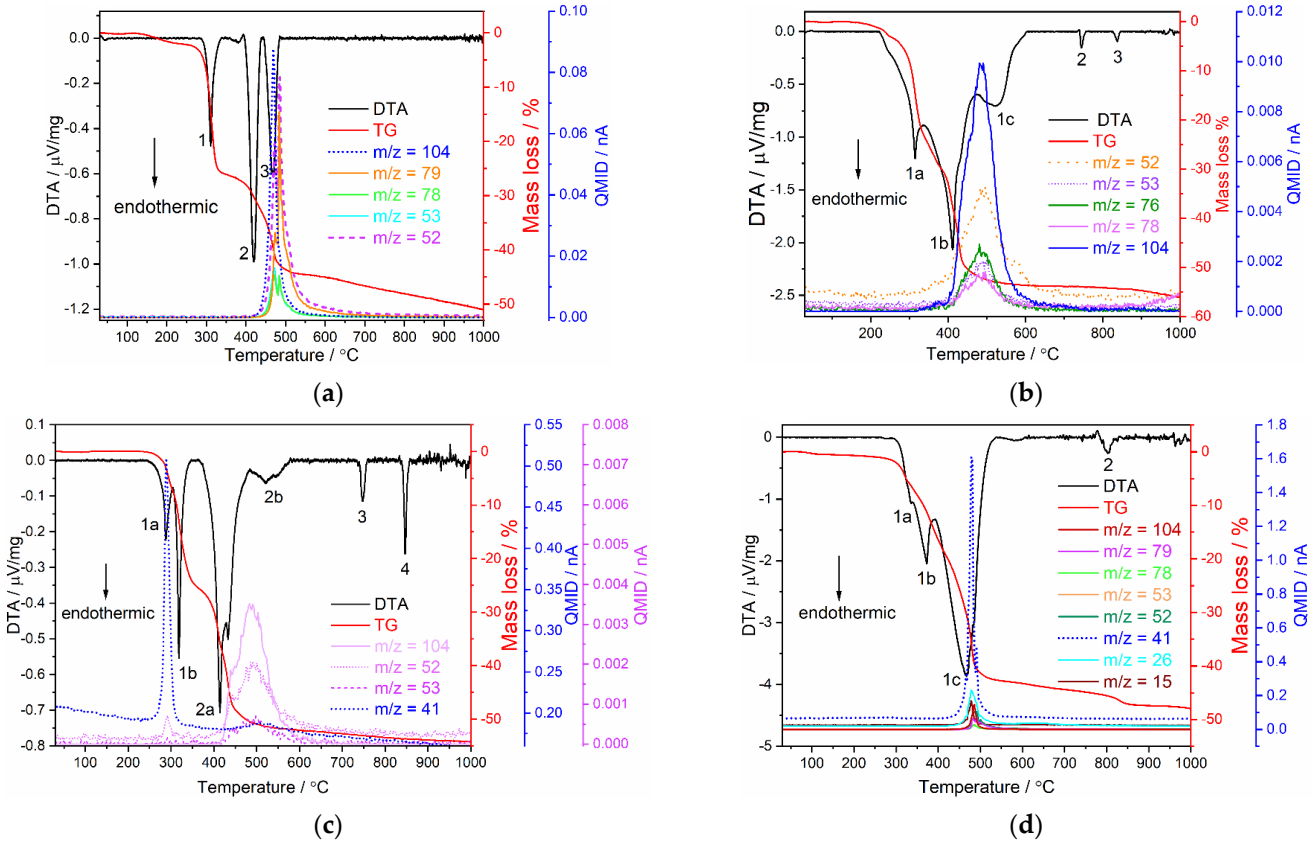

Figure 9. Simultaneous DTA/TG analysis together with mass spectrometry of (**a**) $^{1}{}_{\infty}[Sm_2(2–PyPzH)_4Cl_6]$ (**3**), (**b**) α–$[Eu_2(2–PyPzH)_4Cl_6]$ (**5**), (**c**) β–$[Eu_2(2–PyPzH)_4Cl_6]$ (**9**), and (**d**) $[Tb(2–PyPzH)_2Cl_3]$ (**12**). The investigation was performed in a constant argon flow of 50 mL·min^{-1} with a heating rate of 5 K·min^{-1} from RT to 1000 °C.

For α–$[Eu_2(2–PyPzH)_4Cl_6]$ (**5**) (Figure 9b), two equivalent 2–PyPzH (theoretical mass loss = 52.9%) are released during the combined endothermic signal (1a, 1b, 1c) with a mass loss of 53.7% in the TG and an onset temperature of 230 °C. For β–$[Eu_2(2–PyPzH)_4Cl_6]$ (**9**) (Figure 9c), one equivalent of 2–PyPzH (theoretical mass loss = 26.5%) is released, while the first combined endothermic signal starts at 230 °C (1a, 1b) with a mass loss of 25.8%. The loss of another equivalent 2–PyPzH is evidenced by a 25.6% mass loss during the second combined endothermic signal (2a, 2b). The appearance of two endothermic signals at 745, 835 °C (signals 2, 3) in α–Eu^{3+} (**5**) and at 745, 865 °C (signals 3, 4) in β–Eu^{3+} (**9**), far from the melting point of $EuCl_3$ (theoretical mp = 632 °C) [68], indicates the formation of other phases, confirmed by the lack of $EuCl_3$ reflections and the observation of unknown reflections in the PXRD pattern.

For $[Tb(2–PyPzH)_2Cl_3]$ (**12**) (Figure 9d), the two equivalent 2–PyPzH are not fully released within the combined endothermic signals (1a, 1b, 1c) with a mass loss of 42.9%

(theoretical mass loss = 52.3%) and an onset temperature of 250 °C. A further endothermic signal at 800 °C (signal 2) far from the melting point of $TbCl_3$ (581 °C) [69] is observed beside unknown reflections in the PXRD pattern, indicating the formation of other unknown phases, which cause further mass loss at higher temperatures.

In summary, the 1D-coordination polymer **3** and the monomer complex **12** show the highest stability among the series up to 250 °C, while **5** and **9** are stable up to 230 °C. Further confirmation of the decomposition processes in **3**, **5**, **9**, and **12** was the detection of a set of mass signals at the respective temperatures, which can be assigned to fragments of the ligand ($C_7H_6N^+$ m/z = 104, $C_5H_5N^+$ m/z = 79, $C_5H_2N^+$ m/z = 76, $C_5H_4N^+$ m/z = 78, $C_2HN_2{}^+$ m/z = 53, $C_2N_2{}^+$ m/z = 52, $C_2NH_3{}^+$ m/z = 41, $C_2H_3{}^+$ m/z = 27, $C_2H_2{}^+$ m/z = 26, $CH_3{}^+$ m/z = 15).

3. Materials and Methods

3.1. General Procedures

3–(2–pyridyl)pyrazole (2–PyPzH) was synthesized according to the previously reported procedure [70,71]. The method is described in detail in the Supplementary Materials. The lanthanide chlorides ($NdCl_3$, $SmCl_3$, $EuCl_3$, $TbCl_3$, $HoCl_3$: 99.9%, Sigma Aldrich, St Louis, MO, USA; $DyCl_3$, $GdCl_3$: 99.9%, Strem Chemicals, Newburyport, Massachusetts, United States; $LaCl_3$: 99.9%, Heraeus, Karlsruhe, Germany; $CeCl_3$: 99.9%, abcr, Karlsruhe, Germany) were purchased and used as received. All syntheses involving anhydrous lanthanide chlorides were performed under argon or using a vacuum line, gloveboxes (MBraun Labmaster SP, Innovative Technology PureLab, Garching, Germany), Schlenk tubes, and Duran® glass ampoules (outer ⌀ 10 mm, wall thickness 1.5 mm). Acetonitrile (MeCN), toluene, pyridine, and dichloromethane (DCM) were purified by distillation and dried using standard methods. The solid reactants for the solvothermal reactions were mixed and sealed together with the solvent in an ampoule under reduced pressure ($p = 1.0 \times 10^{-3}$ mbar). A stir bar was added to the reaction mixture when needed. Afterward, the prepared ampoules were placed in heating furnaces (Büchi glass ovens, Büchi Labortechnik, Flawil, Switzerland or heating furnaces based on Al_2O_3 tubes with Kanthal wire resistance heating and NiCr/Ni (Eurotherm 2416) temperature control elements), for which temperature programs and working steps according to the specific synthesis methods were applied. After removing the solvents, the solid raw products were dried at RT in a dynamic vacuum ($p = 1.0 \times 10^{-3}$ mbar) before further steps. The bulk materials were characterized by powder X-ray diffraction (PXRD) and CHN analysis. The infrared spectrum (ATR) of the studied compounds are given in the Supplementary Materials (Figures S39–S51).

3.2. X-ray Crystallography

SCXRD determinations were performed on a Bruker AXS D8 Venture diffractometer (Karlsruhe, Germany) equipped with dual IμS microfocus sources, a collimating Quazar multilayer mirror, a Photon 100 detector, and an Oxford Cryosystems 700 low-temperature system (Mo–K_α radiation; λ = 71.073 pm), except **11**, for which a Bruker AXS D8 Venture diffractometer (Germany) equipped with Photon III–C14 and an Oxford Cryosystems 800 low-temperature system (Mo–K_α radiation; λ = 71.073 pm) was used. For **2** and **18**, the data collections were performed at 200 K because of the cracking behavior of the single crystals upon cooling to 100 K. All other data were collected at 100 K. The structures were solved with direct methods and refined with the least squares method implemented in ShelX [72,73]. All non-hydrogen atoms were refined anisotropically. Hydrogen atoms were assigned to idealized geometric positions and included in structure factor calculations. Further, a ligand molecule (2–PyPzH) in the asymmetric unit of **1**, **2**, **3**, **5**, **6**, **17** and the pyridine solvent in **18** were found to be fully disordered and were refined with the help of restraints to achieve a proper structural model. The structures of **1–3, 5–18** have been deposited to the Cambridge Crystallographic Data Center (CCDC) as supplementary publication No. 2208098 (**1**), 2208099 (**2**), 2208100 (**3**), 2208101 (**5**), 2208102 (**6**), 2208103 (**7**),

2208104 (**8**), 2208105 (**9**), 2208106 (**10**), 2208107 (**11**), 2208108 (**12**), 2208109 (**13**), 2208110 (**14**), 2208111 (**15**), 2208112 (**16**), 2208113 (**17**), and 2208114 (**18**). Crystallographic data and selected interatomic distances are listed in Tables S1–S13 for the investigated compounds.

Depictions of the crystal structures were created with Diamond [74]. Structure overlays for polymorphs **5** and **9** were calculated with Mercury [75].

PXRD analyses of the investigated compounds were carried out on a Stoe Stadi P diffractometer (Darmstadt, Germany) with a focusing Ge(111) monochromator and a Dectris Mythen 1K strip detector in Debye–Scherrer geometry. All powder samples were ground in a mortar and filled into Lindemann glass capillaries with 0.3 mm diameter under an inert gas atmosphere. All samples were measured in transmission geometry with Cu–K_α radiation (λ = 154.056 pm). Data collection was done using the Stoe Powder Diffraction Software Package WinXPOW and Pawley fits on the data were performed using TOPAS Academic [76]. The data are listed in Figures 5 and S6–S11.

3.3. Synthesis

3.3.1. Synthesis of $^1{}_\infty[Ln_2(2–PyPzH)_4Cl_6]$, Ln = La (1), Nd (2), Sm (3)

A mixture of the respective $LnCl_3$ (76 µmol) and 2–PyPzH (158 µmol) in 0.3 mL MeCN was sealed in an evacuated Duran glass ampoule. The solvent was frozen using liquid nitrogen before a vacuum was applied to the ampoule and the ampoule was sealed. For **1** and **2**, the ampoule was heated in a tubular furnace to 160 °C within 24 h. The temperature was held for 24 h and then lowered to 25 °C within another 72 h. For **3**, the phase pure bulk was only achievable in a synthesis upon stirring using a Büchi oven. The furnace temperature was raised to 100 °C and held for 48 h until colorless crystals formed above the level of the solvent, followed by cooling to 25 °C. The obtained colorless crystalline bulk was washed with DCM before the characterization processes via SCXRD, PXRD, IR spectroscopy, and CHN analysis.

$^1{}_\infty[La_2(2–PyPzH)_4Cl_6]$: $C_{16}H_{14}N_6Cl_3La$ (535.59 g·mol^{-1}): C 36.81 (calcd. 35.88); H 3.33 (2.63); N 14.84 (15.69)%. Yield: 80%. FT-IR (ATR): $\tilde{\nu}$ = 3086 (w), 1604 (s), 1569 (w), 1531 (w), 1500 (m), 1456 (m), 1440 (w), 1426 (m), 1356 (m), 1289 (w), 1242 (w), 1181 (w), 1156 (m), 1136 (w), 1085 (s), 1058 (s), 1004 (m), 964 (m), 927 (w), 894 (w), 802 (w), 775 (s), 741 (w), 710 (m), 634 (m), 614 (w), 505 (w), 465 (w) cm^{-1}.

$^1{}_\infty[Nd_2(2–PyPzH)_4Cl_6]$: $C_{16}H_{14}N_6Cl_3Nd$ (540.92 g·mol^{-1}): C 34.87 (calcd. 35.53); H 2.52 (2.61); N 15.35 (15.54)%. Yield: 84%. FT-IR (ATR): $\tilde{\nu}$ = 3129 (w), 1605 (m), 1568 (w), 1531 (w), 1501 (m), 1456 (m), 1440 (m), 1426 (m), 1358 (m), 1290 (w), 1242 (w), 1181 (m), 1155 (m), 1138 (m), 1107 (w), 1085 (m), 1057 (m), 1005 (m), 964 (m), 927 (w), 892 (w), 801 (m), 773 (s), 742 (m), 710 (m), 634 (m), 614 (m), 506 (w), 467 (w) cm^{-1}.

$^1{}_\infty[Sm_2(2–PyPzH)_4Cl_6]$: $C_{16}H_{14}N_6Cl_3Sm$ (547.03 g·mol^{-1}): C 35.06 (calcd. 35.13); H 2.46 (2.58); N 15.85 (15.36)%. Yield: 86%. FT-IR (ATR): $\tilde{\nu}$ = 3123 (w), 1638 (w), 1607 (m), 1596 (w),1503 (w), 1457 (w), 1428 (m), 1361 (m), 1292 (w), 1247 (w), 1183 (w), 1157 (w), 1140 (w), 1087 (m), 1059 (m), 1006 (w), 966 (m), 928 (w), 774 (s), 743 (w), 710 (w), 635 (m), 615 (w), 507 (w), 468 (w) cm^{-1}.

3.3.2. Synthesis of α–$[Ln_2(2–PyPzH)_4Cl_6]$, Ln = Sm (4), Eu (5), Gd (6)

A mixture of the respective $LnCl_3$ (138 µmol) and 2–PyPzH (276 µmol) in 0.3 mL MeCN in **5** and **6** or toluene in **4** was prepared and sealed in an evacuated Duran glass ampoule. For **4**, the tubular furnace was heated to 120 °C within 24 h. The temperature was held for 72 h and then lowered to 25 °C within another 48 h. For **5** and **6**, phase pure bulk was achieved by stirring while using a Büchi oven. The furnace temperature was raised to 100 °C and held for 24 h until colorless crystals formed above the level of the solvent, followed by cooling to 25 °C. Colorless single crystals of the products (**6** and **7**) were selected for SCXRD measurements.

α–$[Sm_2(2–PyPzH)_4Cl_6]$: $C_{16}H_{14}N_6Cl_3Sm$ (547.03 g·mol^{-1}): C 34.71 (calcd. 35.13); H 2.55 (2.58); N 15.17 (15.36)%. Yield: 89%. FT-IR (ATR): $\tilde{\nu}$ = 3047 (w), 1602 (m), 1568 (w), 1532 (w), 1501 (m), 1459 (m), 1446 (w), 1427 (m), 1369 (w), 1295 (w), 1247 (w), 1190 (m),

1160 (w), 1141 (m), 1109 (w), 1087 (m), 1058 (m), 1004 (m), 966 (m), 929 (m), 898 (w), 812 (m), 784 (s), 768 (s), 705 (m), 676 (w), 632 (m), 611 (m), 510 (w), 471 (w) cm^{-1}.

α–[Eu_2(2–PyPzH)$_4Cl_6$]: $C_{16}H_{14}N_6Cl_3Eu$ (548.64 g·mol^{-1}): C 35.90 (calcd. 35.03); H 3.30 (2.57); N 14.42 (15.32)%. Yield: 87%. FT-IR (ATR): $\tilde{\nu}$ = 3115 (w), 1602 (m), 1568 (w), 1501 (w), 1460 (m), 1427 (w), 1369 (w), 1292 (w), 1247 (w), 1190 (m), 1161 (w), 1141 (w), 1087 (m), 1058 (m), 1005 (m), 966 (m), 930 (w), 812 (w), 784 (s), 768 (s), 705 (m), 675 (w), 632 (m), 611 (m), 510 (w), 470 (w) cm^{-1}.

α–[Gd_2(2–PyPzH)$_4Cl_6$]: $C_{16}H_{14}N_6Cl_3Gd$ (553.93 g·mol^{-1}): C 34.21 (calcd. 34.69); H 2.48 (2.55); N 14.47 (15.17)%. Yield: 82%. FT-IR (ATR): $\tilde{\nu}$ = 3123 (w), 1628 (w), 1602 (m), 1568 (w), 1502 (m), 1427 (m), 1361 (w), 1292 (w), 1246 (w), 1185 (w), 1161 (w), 1139 (w), 1087 (m), 1059 (m), 1005 (m), 966 (m), 928 (w), 897 (w), 767 (s), 710 (s), 632 (m), 610 (m), 469 (w) cm^{-1}.

3.3.3. Synthesis of β–[Ln_2(2–PyPzH)$_4Cl_6$], Ln = Sm (8), Eu (9)

A mixture of the respective $LnCl_3$ (138 µmol) and 2–PyPzH (276 µmol) in 0.3 mL MeCN was sealed in an evacuated glass ampoule after freezing the solvent. A Büchi oven with a stirrer was used to raise the temperature of the ampoule to 160 °C and held for three days until colorless crystals formed above the solvent level, followed by cooling to 25 °C. Appropriate colorless single crystals were then selected for SCXRD measurements. The bulk was characterized by PXRD, IR spectroscopy, and CHN analysis

β–[Sm_2(2–PyPzH)$_4Cl_6$]: $C_{16}H_{14}N_6Cl_3Sm$ (547.03 g·mol^{-1}): C 34.45 (calcd. 35.13); H 2.07 (2.58); N 14.99 (15.36)%. Yield: 85%. FT-IR (ATR): $\tilde{\nu}$ = 3056 (w), 1605 (m), 1568 (w), 1531 (w), 1499 (m), 1459 (m), 1444 (w), 1427 (m), 1366 (w),1294 (w), 1425 (w), 1188 (m), 1142 (m), 1109 (w), 1089 (s), 1059 (m), 1004 (w), 966 (m), 928 (w), 896 (w), 806 (w), 781 (s), 771 (s), 704 (s), 676 (m), 633 (m), 610 (s), 507 (w), 470 (w) cm^{-1}.

β–[Eu_2(2–PyPzH)$_4Cl_6$]: $C_{16}H_{14}N_6Cl_3Eu$ (548.64 g·mol^{-1}): C 34.22 (calcd. 35.03); H 1.71 (2.57); N 14.50 (15.32)%. Yield: 92%. FT-IR (ATR): $\tilde{\nu}$ = 3112 (w), 1681 (w), 1605 (m), 1568 (m), 1531 (w), 1499 (m), 1458 (m), 1440 (w), 1427 (m), 1362 (w), 1291 (w), 1244 (w), 1184 (m), 1153 (w), 1142 (m), 1109 (w), 1088 (s), 1059 (m), 1004 (m), 965 (m), 929 (w), 895 (w), 806 (w), 781 (s), 771 (s), 704 (s), 677 (m), 632 (m), 610 (m), 508 (w), 471 (w) cm^{-1}.

3.3.4. Synthesis of [Ce(2–PyPzH)$_3Cl_3$] (11)

A mixture of $CeCl_3$ (77 µmol) and 2–PyPzH (241 µmol) in 0.3 mL MeCN was sealed in an evacuated glass ampoule after freezing the solvent using liquid nitrogen. The ampoule was heated to 90 °C in 1 h and then 160 °C within 24 h. The temperature was held for 24 h and then lowered to 25 °C within 72 h. The obtained colorless crystalline bulk was washed with DCM before the characterization process using SCXRD, PXRD, IR spectroscopy, and CHN analysis. $C_{24}H_{21}N_9Cl_3Ce$ (681.97 g·mol^{-1}): C 43.15 (calcd. 42.27); H 3.90 (3.10); N 17.54 (18.48)%. Yield: 90%. FT-IR (ATR): $\tilde{\nu}$ = 3152 (w), 1633 (w), 1601 (m), 1567 (w), 1529 (w), 1500 (m), 1455 (m), 1440 (m), 1421 (m), 1358 (w), 1302 (w), 1283 (w), 1240 (w), 1189 (m), 1151 (w), 1138 (m), 1105 (w), 1086 (m), 1055 (m), 1002 (w), 959 (m), 928 (w), 909 (w), 762 (s), 713 (m), 686 (w), 629 (m), 615 (m), 595 (w), 515 (w), 466 (w) cm^{-1}.

3.3.5. Synthesis of [Ln(2–PyPzH)$_2Cl_3$], Ln = Tb (12), Dy (13), Ho (14), Er (15)

A mixture of the respective $LnCl_3$ (80 µmol) and 2–PyPzH (175 µmol) in 0.6 mL MeCN was sealed in an evacuated Duran glass ampoule after freezing the solvent. The ampoule was heated in a tubular furnace to 160 °C within 48 h. The temperature was held for 72 h and then lowered to 25 °C within another 96 h. The obtained colorless crystalline bulk was washed with DCM before the characterization process using SCXRD, PXRD, IR spectroscopy, and CHN analysis.

[Tb(2–PyPzH)$_2Cl_3$]: $C_{16}H_{14}N_6Cl_3Tb$ (555.60 g·mol^{-1}): C 33.95 (calcd. 34.59); H 2.37 (2.54); N 14.75 (15.13)%. Yield: 93%. FT-IR (ATR): $\tilde{\nu}$ = 3117 (w), 1601 (m), 1565 (w), 1536 (w), 1509 (m), 1469 (m), 1342 (m), 1368 (w), 1295 (w), 1244 (w), 1208 (m), 1159 (w),

1138 (w), 1111 (w), 1089 (m), 1055 (w), 1012 (m), 969 (m), 931 (w), 886 (w), 789 (m), 761 (s), 701 (m), 668 (m), 635 (m), 599 (m), 504 (w), 473 (w) cm^{-1}.

[Dy(2–PyPzH)$_2$Cl$_3$]: $C_{16}H_{14}N_6Cl_3Dy$ (559.18 g·mol^{-1}): C 34.96 (calcd. 34.37); H 2.41 (2.52); N 14.51 (15.03)%. Yield: 90%. FT-IR (ATR): $\tilde{\nu}$ = 3117 (w), 1602 (m), 1566 (w), 1536 (w), 1510 (m), 1469 (m), 1432 (m), 1369 (w), 1296 (w), 1244 (w), 1208 (m), 1159 (w), 1139 (m), 1112 (w), 1090 (m), 1056 (w), 1013 (m), 967 (m), 931 (w), 886 (w), 790 (m), 762 (s), 755 (s), 702 (m), 669 (m), 635 (m), 600 (m), 505 (w), 474 (w) cm^{-1}.

[Ho(2–PyPzH)$_2$Cl$_3$]: $C_{16}H_{14}N_6Cl_3Ho$ (561.61 g·mol^{-1}): C 33.60 (calcd. 34.22); H 2.33 (2.51); N 14.14 (14.96)%. Yield: 94%. FT-IR (ATR): $\tilde{\nu}$ = 3117 (w), 1602 (m), 1566 (w), 1536 (w), 1510 (m), 1468 (m), 1432 (m), 1369 (m), 1295 (m), 1244 (m), 1208 (m), 1159 (m), 1139 (m), 1112 (m), 1090 (m), 1056 (m), 1013 (m), 970 (m), 931 (w), 888 (w), 789 (m), 760 (s), 701 (m), 668 (m), 635 (m), 599 (m), 504 (w), 475 (w) cm^{-1}.

[Er(2–PyPzH)$_2$Cl$_3$]: $C_{16}H_{14}N_6Cl_3Er$ (563.94 g·mol^{-1}): C 33.53 (calcd. 34.08); H 2.08 (2.50); N 14.24 (14.90)%. Yield: 88%. FT-IR (ATR): $\tilde{\nu}$ = 3074 (w), 1604 (m), 1565 (m), 1537 (w), 1510 (m), 1469 (m), 1432 (m), 1370 (m), 1297 (m), 1245 (m), 1209 (m), 1159 (m), 1140 (m), 1089 (m), 1012 (m), 970 (m), 931 (m), 886 (w), 760 (s), 701 (m), 669 (m), 635 (m), 600 (m), 504 (w), 475 (w) cm^{-1}.

3.3.6. Single Crystals of α–[Tb$_2$(2–PyPzH)$_4$Cl$_6$] (7)

A mixture of $TbCl_3$ (19 μmol) and 2–PyPzH (59 μmol) in 0.3 mL MeCN was sealed in an evacuated glass ampoule after freezing the solvent. The ampoule was heated in a furnace to 160 °C within 48 h. The temperature was held for 72 h and then lowered to 25 °C within another 96 h. A colorless single crystal of the product was selected for SCXRD measurement.

3.3.7. Single Crystals of β–[Gd$_2$(2–PyPzH)$_4$Cl$_6$] (10)

A mixture of $GdCl_3$ (138 μmol) and 2–PyPzH (276 μmol) in 0.1 mL MeCN was sealed in an evacuated glass ampoule after freezing the solvent. The ampoule was heated in a Büchi oven to 160 °C by stirring until colorless crystals formed above the level of the solvent, followed by cooling to 25 °C. A colorless single crystal of the product was selected for SCXRD measurement.

3.3.8. Single Crystals of [Gd$_2$(2–PyPzH)$_3$(2–PyPz)Cl$_5$] (16) and [Gd$_3$(2–PyPzH)$_8$Cl$_8$]Cl (17)

A mixture of the respective $LnCl_3$ (138 μmol) and 2–PyPzH (276 μmol) in 0.3 mL MeCN was sealed in an evacuated glass ampoule after freezing the solvent. The ampoule was heated in a tubular furnace to 160 °C within 48 h. The temperature was held for 72 h and then lowered to 25 °C within another 24 h. A colorless single crystal of the product was selected for SCXRD measurement.

3.3.9. Single Crystals of [PyH][Tb(2–PyPzH)$_2$Cl$_4$] (18)

A mixture of $TbCl_3$ (19 μmol) and 2–PyPzH (59 μmol) in 0.1 mL pyridine was sealed in an evacuated glass ampoule after freezing the solvent. The ampoule was heated in a tubular furnace to 100 °C within 72 h. The temperature was held for 72 h and then lowered to 25 °C within another 96 h. A highly reflective colorless single crystal of the product was selected for the SCXRD measurement.

4. Conclusions

A novel Ce^{3+}-based orange-emitting material was synthesized from anhydrous $CeCl_3$ together with the ligand 3–(2–pyridyl)pyrazole (2–PyPzH). The obtained [Ce(2–PyPzH)$_3$Cl$_3$] represents the first undoped Ce^{3+} phosphor material to show intense orange emission based on 5d–4f transitions. This marks the presented compound an exception within other Ce^{3+}-based emitters. [Tb(2–PyPzH)$_2$Cl$_3$] exhibits high luminescence efficiency with a quantum yield of 92%, reflecting an excellent antenna effect through ligand-to-metal energy transfer. A great structural diversity has been observed along the lanthanide se-

ries, from 1D-coordination polymers through dimers to monomer complexes, all of which have been synthesized and characterized that are all luminescent. Two polymorphs are found for each Sm^{3+}, Eu^{3+}, and Gd^{3+} and the α-phase crystallizes at lower temperatures in the $P2_1/c$, while the β-phase crystallizes in the $P\bar{1}$ space group. The Ln^{3+} ions exhibit a change in coordination number from nine in Ce^{3+} to seven in Tb^{3+}, Dy^{3+}, Ho^{3+}, and Er^{3+} ions. The characterization of the new compounds was achieved by SC and PXRD, elemental analysis, IR, photoluminescence spectroscopy, and thermal analysis. Overall, this shows the high potential of coordination polymers and complexes with a pyridyl-pyrazole ligand as the N-donor for the design of materials with versatile structures as well as photophysical properties.

Supplementary Materials: The following supporting information can be downloaded at: https://www.mdpi.com/article/10.3390/inorganics10120254/s1, additional experimental details; Tables S1–S13: Crystallographic data and selected interatomic distances (pm) and angles (○) of $^1{}_\infty[Ln_2(2–PyPzH)_4Cl_6]$, Ln = La (**1**), Nd (**2**), Sm (**3**), α–$[Ln_2(2–PyPzH)_4Cl_6]$, Ln = Eu (**5**), Gd (**6**), Tb (**7**), β–$[Ln_2(2–PyPzH)_4Cl_6]$, Ln = Sm (**8**), Eu (**9**), Gd (**10**), $[Ce(2–PyPzH)_3Cl_3]$ (**11**), $[Ln(2–PyPzH)_2Cl_3]$, Ln = Tb (**12**), Dy (**13**), Ho (**14**), Eu (**15**), $[Gd_2(2–PyPzH)_3(2–PyPz)Cl_5]$ (**16**), $[Gd_3(2–PyPzH)_8Cl_8]Cl$ (**17**), and $[PyH][Tb(2–PyPzH)_2Cl_4]$ (**18**); Figure S1: (**a**) Extended coordination sphere of Tb^{3+} ion in α–$[Tb_2(2–PyPzH)_4Cl_6]$ (**7**) representing the isotypic complexes **4**–**7**. (**b**) Packing structure of **7** with a view along [100]. In all figures, the hydrogen atoms are omitted for clarity and the coordination polyhedra around Ln^{3+} are indicated in green, with thermal ellipsoids shown with a probability of 50%; Figure S2: Overlay of the molecular structures of α–$[Eu_2(2–PyPzH)_4Cl_6]$ (red) (**5**) and β–$[Eu_2(2–PyPzH)_4Cl_6]$ (blue) (**9**); Figure S3: (**a**) Extended coordination sphere of Gd^{3+} ion in $[Gd_2(2–PyPzH)_3(2–PyPz)Cl_5]$ (**16**). (**b**) Packing structure of **16** with a view along [100]; Figure S4: (**a**) Extended coordination sphere of Gd^{3+} ion in $[Gd_3(2–PyPzH)_8Cl_8]Cl$ (**17**). (**b**) Packing structure of **17** with a view along [100]; Figure S5: (**a**) Extended coordination sphere of Tb^{3+} ion in $[PyH][Tb(2–PyPzH)_2Cl_4]$ (**18**). (**b**) Packing structure of **18** with a view along [100], the protonated pyridine molecules were omitted for clarity. Symmetry operation: I -x+1,y,-z+3/2; Figures S6–S9 Comparison of the observed powder X-ray diffraction pattern (colored) of $^1{}_\infty[Ln_2(2–PyPzH)_4Cl_6]$, RE = La (**1**), Nd (**2**), Sm (**3**), α–$[Ln_2(2–PyPzH)_4Cl_6]$, Ln = Sm (**4**), Eu (**5**), Gd (**6**), β–$[Ln_2(2–PyPzH)_4Cl_6]$, Ln = Sm (**8**), Eu (**9**), and $[Ln(2–PyPzH)_2Cl_3]$, Ln = Tb (**12**), Dy (**13**), Ho (**14**), Er (**15**) with the corresponding simulated diffraction patterns from the single crystal X-ray data (black) for each case; Figure S10: Pawley refinement of (**a**) β–$[Sm_2(2–PyPzH)_4Cl_6]$ (**8**) with a GOF of 1.16, (**b**) $[Ce(2–PyPzH)_3Cl_3]$ (**11**) with a GOF of 1.87. The experimental data are shown in black, Pawley fit in red, the corresponding difference plot in blue, and the hkl position markers in green; Figure S11: Comparison of the observed powder X-ray diffraction pattern (colored) of a mixture of α–$[Gd_2(2–PyPzH)_4Cl_6]$ (**6**) and β–$[Gd_2(2–PyPzH)_4Cl_6]$ (**10**) with the simulated diffraction pattern from the single crystal X-ray data of **6** and **10** (black); Figures S12–S24: Absorption spectra of 2–PyPzH, $^1{}_\infty[Ln_2(2–PyPzH)_4Cl_6]$, Ln=La (**1**), Nd (**2**), Sm (**3**), α–$[Ln_2(2–PyPzH)_4Cl_6]$, Ln=Eu (**5**), Gd (**6**), β–$[Ln_2(2–PyPzH)_4Cl_6]$, Ln=Sm (**8**), Eu (**9**), $[Ce(2–PyPzH)_3Cl_3]$ (**11**), $[Ln(2–PyPzH)_2Cl_3]$, Ln=Tb (**12**), Dy (**13**), Ho (**14**), Er (**15**) in the solid state at room temperature; Figures S25–S38: Normalized excitation and emission spectra of 2–PyPzH, $^1{}_\infty[Ln_2(2–PyPzH)_4Cl_6]$, Ln=La (**1**), Nd (**2**), Sm (**3**), α–$[Ln_2(2–PyPzH)_4Cl_6]$, Ln=Sm (**4**), Eu (**5**), Gd (**6**), β–$[Ln_2(2–PyPzH)_4Cl_6]$, Ln=Sm (**8**), Eu (**9**), $[Ce(2–PyPzH)_3Cl_3]$ (**11**), and $[Ln(2–PyPzH)_2Cl_3]$, Ln=Tb (**12**), Dy (**13**), Ho (**14**), Er (**15**) at room temperature (top) and 77 K (bottom). Wavelengths at which the spectra were recorded are reported in the legends; Figures S39–S51: The infrared spectrum (ATR) of $^1{}_\infty[Ln_2(2–PyPzH)_4Cl_6]$, Ln=La (**1**), Nd (**2**), Sm(**3**), α–$[Ln_2(2–PyPzH)_4Cl_6]$, Ln=Sm (**4**), Eu (**5**), Gd (**6**), β–$[Ln_2(2–PyPzH)_4Cl_6]$, Ln=Sm (**8**), Eu (**9**), $[Ce(2–PyPzH)_3Cl_3]$ (**11**), and $[Ln(2–PyPzH)_2Cl_3]$, Ln=Tb (**12**), Dy (**13**), Ho (**14**), Er (**15**). Reference [77] is cited in the Supplementary Materials.

Author Contributions: Conceptualization, K.M.-B. and H.Y.; methodology, H.Y. and A.E.S.; software, H.Y. and J.B.; validation, H.Y.; formal analysis, H.Y., A.E.S. and J.B.; investigation, H.Y.; resources, I.V.T. and K.M.-B.; data curation, H.Y. and J.B.; writing—original draft preparation, H.Y.; writing—review and editing, H.Y., A.E.S., J.B., I.V.T. and K.M.-B.; visualization, H.Y.; supervision, K.M.-B.; project administration, K.M.-B.; All authors have read and agreed to the published version of the manuscript.

Funding: This research was funded by the Volkswagen Foundation within the project "Molecular materials—bridging magnetism and luminescence." Heba Youssef was awarded a PhD fellowship by the Egyptian Ministry of Higher Education (MoHE) and the German Academic Exchange Service (DAAD) within the German Egyptian Research Long-term Scholarship (GERLS) Program, 2017 (57311832), the funding agency is the German Academic Exchange Service Cairo. The synthesis of the studied ligand was funded by the Russian Science Foundation (project № 19–13–00272).

Data Availability Statement: CCDC 2208098 (**1**), 2208099 (**2**), 2208100 (**3**), 2208101 (**5**), 2208102 (**6**), 2208103 (**7**), 2208104 (**8**), 2208105 (**9**), 2208106 (**10**), 2208107 (**11**), 2208108 (**12**), 2208109 (**13**), 2208110 (**14**), 2208111 (**15**), 2208112 (**16**), 2208113 (**17**), 2208114 (**18**) contain the supplementary crystallographic data for this paper. These data can be obtained free of charge via http://www.ccdc.cam.ac.uk/conts/retrieving.html (or from the CCDC, 12 Union Road, Cambridge CB2 1EZ, UK; Fax: +44 1223 336033; email: deposit@ccdc.cam.ac.uk).

Conflicts of Interest: The authors declare no conflict of interest.

References

1. Forsberg, J.H. Complexes of lanthanide(III) ions with nitrogen donor ligands. *Coord. Chem. Rev.* **1973**, *10*, 195–226. [CrossRef]
2. Youssef, H.; Schäfer, T.C.; Becker, J.; Sedykh, A.E.; Basso, L.; Pietzonka, C.; Taydakov, I.V.; Kraus, F.; Müller-Buschbaum, K. 3D-Frameworks and 2D-networks of lanthanide coordination polymers with 3-pyridylpyrazole: Photophysical and magnetic properties. *Dalton Trans.* **2022**, *51*, 14673–14685. [CrossRef] [PubMed]
3. Drew, M.G.; Foreman, M.R.S.; Hudson, M.J.; Kennedy, K.F. Structural studies of lanthanide complexes with tetradentate nitrogen ligands. *Inorg. Chim. Acta* **2004**, *357*, 4102–4112. [CrossRef]
4. Miguirditchian, M.; Guillaneux, D.; François, N.; Airvault, S.; Ducros, S.; Thauvin, D.; Madic, C.; Illemassène, M.; Lagarde, G.; Krupa, J.C. Complexation of lanthanide(III) and actinide(III) cations with tridentate nitrogen-donor ligands: A luminescence and spectrophotometric study. *Nucl. Sci. Eng.* **2006**, *153*, 223–232. [CrossRef]
5. Sedykh, A.E.; Bissert, R.; Kurth, D.G.; Müller-Buschbaum, K. Structural diversity of salts of terpyridine derivatives with europium(III) located in both, cation and anion, in comparison to molecular complexes. *Z. Kristallogr. Cryst. Mater.* **2020**, *235*, 353–363. [CrossRef]
6. Höller, C.J.; Mai, M.; Feldmann, C.; Müller-Buschbaum, K. The interaction of rare earth chlorides with 4,4′-bipyridine for the reversible formation of template based luminescent Ln-N-MOFs. *Dalton Trans.* **2010**, *39*, 461–468. [CrossRef]
7. Youssef, H.; Sedykh, A.E.; Becker, J.; Schäfer, T.; Taydakov, I.V.; Li, H.R.; Müller-Buschbaum, K. Variable luminescence and chromaticity of homoleptic frameworks of the lanthanides together with pyridylpyrazolates. *Chem. Eur. J.* **2021**, *27*, 16634–16641. [CrossRef]
8. Sedykh, A.E.; Kurth, D.G.; Müller-Buschbaum, K. Two series of lanthanide coordination polymers and complexes with 4′-phenylterpyridine and their luminescence properties. *Eur. J. Inorg. Chem.* **2019**, *2019*, 4564–4571. [CrossRef]
9. Piguet, C.; Williams, A.F.; Bernardinelli, G.; Buenzli, J.C.G. Structural and photophysical properties of lanthanide complexes with planar aromatic tridentate nitrogen ligands as luminescent building blocks for triple-helical structures. *Inorg. Chem.* **1993**, *32*, 4139–4149. [CrossRef]
10. Ekberg, C.; Fermvik, A.; Retegan, T.; Skarnemark, G.; Foreman, M.; Hudson, M.; Englund, S.; Nilsson, M. An overview and historical look back at the solvent extraction using nitrogen donor ligands to extract and separate An(III) from Ln(III). *Radiochim. Acta* **2008**, *96*, 225–233. [CrossRef]
11. Matthes, P.R.; Schönfeld, F.; Zottnick, S.H.; Müller-Buschbaum, K. Post-synthetic shaping of porosity and crystal structure of Ln-Bipy-MOFs by thermal treatment. *Molecules* **2015**, *20*, 12125–12153. [CrossRef] [PubMed]
12. Meihaus, K.R.; Minasian, S.G.; Lukens, W.W., Jr.; Kozimor, S.A.; Shuh, D.K.; Tyliszczak, T.; Long, J.R. Influence of pyrazolate vs. N-heterocyclic carbene ligands on the slow magnetic relaxation of homoleptic trischelate lanthanide(III) and uranium(III) complexes. *J. Am. Chem. Soc.* **2014**, *136*, 6056–6068. [CrossRef]
13. Hassan, S.S.; Mohamed, E.F. Antimicrobial, antioxidant and antitumor activities of nano-structure Eu(III) and La(III) complexes with nitrogen donor tridentate ligands. *Appl. Organomet. Chem.* **2020**, *34*, e5258. [CrossRef]
14. Bünzli, J.-C.G.; Eliseeva, S.V. Basics of lanthanide photophysics. In *Springer Series on Fluorescence: Lanthanide Luminescence: Photophysical, Analytical and Biological Aspects*; Wolfbeis, O.S., Hof, M., Eds.; Springer: Berlin/Heidelberg, Germany, 2011; Volume 7, pp. 1–46.
15. Yin, H.; Carroll, P.J.; Anna, J.M.; Schelter, E.J. Luminescent Ce(III) complexes as stoichiometric and catalytic photoreductants for halogen atom abstraction reactions. *J. Am. Chem. Soc.* **2015**, *137*, 9234–9237. [CrossRef] [PubMed]
16. Qiao, Y.; Sergentu, D.-C.; Yin, H.; Zabula, A.V.; Cheisson, T.; McSkimming, A.; Manor, B.C.; Carroll, P.J.; Anna, J.M.; Autschbach, J.; et al. Understanding and controlling the emission brightness and color of molecular cerium luminophores. *J. Am. Chem. Soc.* **2018**, *140*, 4588–4595. [CrossRef] [PubMed]
17. Lindqvist-Reis, P.; Réal, F.; Janicki, R.; Vallet, V. Unraveling the ground state and excited state structures and dynamics of hydrated Ce^{3+} ions by experiment and theory. *Inorg. Chem.* **2018**, *57*, 10111–10121. [CrossRef]

18. Wang, L.; Zhao, Z.; Zhan, G.; Fang, H.; Yang, H.; Huang, T.; Zhang, Y.; Jiang, N.; Duan, L.; Liu, Z.; et al. Deep-blue organic light-emitting diodes based on a doublet *d–f* transition cerium(III) complex with 100% exciton utilization efficiency. *Light Sci. Appl.* **2020**, *9*, 157. [CrossRef]
19. Zhao, Z.; Wang, L.; Zhan, G.; Liu, Z.; Bian, Z.; Huang, C. Efficient rare earth cerium(III) complex with nanosecond $d-f$ emission for blue organic light-emitting diodes. *Natl. Sci. Rev.* **2021**, *8*, nwaa193. [CrossRef]
20. Qin, X.; Liu, X.; Huang, W.; Bettinelli, M.; Liu, X. Lanthanide-activated phosphors based on 4f-5d optical transitions: Theoretical and experimental aspects. *Chem. Rev.* **2017**, *117*, 4488–4527. [CrossRef]
21. Yin, H.; Carroll, P.J.; Manor, B.C.; Anna, J.M.; Schelter, E.J. Cerium photosensitizers: Structure–function relationships and applications in photocatalytic aryl coupling reactions. *J. Am. Chem. Soc.* **2016**, *138*, 5984–5993. [CrossRef]
22. Matthes, P.R.; Müller-Buschbaum, K. Synthesis and characterization of the cerium(III) UV-emitting 2D-coordination polymer $^{2\infty}[Ce_2Cl_6(4,4'\text{-bipyridine})_4]\cdot$py. *Z. Anorg. Allg. Chem.* **2014**, *640*, 2847–2851. [CrossRef]
23. Meyer, L.V.; Schönfeld, F.; Zurawski, A.; Mai, M.; Feldmann, C.; Müller-Buschbaum, K. A blue luminescent MOF as a rapid turn-off/turn-on detector for H_2O, O_2 and CH_2Cl_2, MeCN: $^{3}{}_{\infty}[Ce(Im)_3ImH]\cdot$ImH. *Dalton Trans.* **2015**, *44*, 4070–4079. [CrossRef] [PubMed]
24. Bünzli, J.-C.G. On the design of highly luminescent lanthanide complexes. *Coord. Chem. Rev.* **2015**, *293*, 19–47. [CrossRef]
25. Eliseeva, S.V.; Bünzli, J.-C.G. Lanthanide luminescence for functional materials and bio-sciences. *Chem. Soc. Rev.* **2010**, *39*, 189–227. [CrossRef] [PubMed]
26. Weissman, S. Intramolecular energy transfer the fluorescence of complexes of europium. *J. Chem. Phys.* **1942**, *10*, 214–217. [CrossRef]
27. Crosby, G.; Whan, R.; Alire, R. Intramolecular energy transfer in rare earth chelates. Role of the triplet state. *J. Chem. Phys.* **1961**, *34*, 743–748. [CrossRef]
28. Frey, S.T.; Horrocks, W.D., Jr. Complexation, luminescence, and energy transfer of Ce^{3+} with a series of multidentate amino phosphonic acids in aqueous solution. *Inorg. Chem.* **1991**, *30*, 1073–1079. [CrossRef]
29. Blasse, G.; Grabmaier, B.C. A general introduction to luminescent materials. In *Luminescent Materials*; Springer: Berlin/Heidelberg, Germany, 1994; pp. 1–9.
30. Fang, P.; Wang, L.; Zhan, G.; Yan, W.; Huo, P.; Ying, A.; Zhang, Y.; Zhao, Z.; Yu, G.; Huang, Y.; et al. Lanthanide cerium(III) tris(pyrazolyl)borate complexes: Efficient blue emitters for doublet organic light-emitting diodes. *ACS Appl. Mater. Interfaces* **2021**, *13*, 45686–45695. [CrossRef]
31. Kodama, N.; Tanii, Y.; Yamaga, M. Optical properties of long-lasting phosphorescent crystals Ce^{3+}-doped $Ca_2Al_2SiO_7$ and $CaYAl_3O_7$. *J. Lumin.* **2000**, *87*, 1076–1078. [CrossRef]
32. Kim, G.C.; Park, H.L.; Yun, S.I.; Moon, B.G. Solid solubility limit of cerium in CaS:Ce^{3+} phosphor. *J. Mater. Sci. Lett.* **1986**, *5*, 359–360. [CrossRef]
33. Van Krevel, J.W.H.; Hintzen, H.T.; Metselaar, R.; Meijerink, A. Long wavelength Ce^{3+} emission in Y–Si–O–N materials. *J. Alloys Compd.* **1998**, *268*, 272–277. [CrossRef]
34. Gauthier, G.; Jobic, S.; Evain, M.; Koo, H.-J.; Whangbo, M.-H.; Fouassier, C.; Brec, R. Syntheses, structures, and optical properties of yellow Ce_2SiS_5, $Ce_6Si_4S_{17}$, and $Ce_4Si_3S_{12}$ materials. *Chem. Mater.* **2003**, *15*, 828–837. [CrossRef]
35. Blasse, G.; Bril, A. A new phosphor for flying-spot cathode-ray tubes for color television: Yellow-emitting $Y_3Al_5O_{12}$–Ce^{3+}. *Appl. Phys. Lett.* **1967**, *11*, 53–55. [CrossRef]
36. Wu, D.; Hao, Z.; Zhang, X.; Pan, G.-H.; Luo, Y.; Zhang, L.; Zhao, H.; Zhang, J. Efficient energy back transfer from Ce^{3+} 5d state to Pr^{3+} $^1D_2$ level in $Lu_3Al_5O_{12}$ upon Pr^{3+} 4f5d excitation. *J. Lumin.* **2017**, *186*, 170–174. [CrossRef]
37. Peng, D.A.I.; Cheng, J.I.; Liming, S.H.E.N.; Qi, Q.I.A.N.; Guobiao, G.U.O.; Zhang, X.; Ningzhong, B.A.O. Photoluminescence properties of YAG: Ce^{3+},Pr^{3+} nano-sized phosphors synthesized by a modified co-precipitation method. *J. Rare Earths* **2017**, *35*, 341–346. [CrossRef]
38. Zeng, P.; Wei, X.; Zhou, S.; Yin, M.; Chen, Y. Evaluation of critical distances for energy transfer between Pr^{3+} and Ce^{3+} in yttrium aluminium garnet. *J. Appl. Phys.* **2016**, *120*, 093104. [CrossRef]
39. Ogiegło, J.M.; Zych, A.; Jüstel, T.; Meijerink, A.; Ronda, C.R. Luminescence and energy transfer in $Lu_3Al_5O_{12}$ scintillators co-doped with Ce^{3+} and Pr^{3+}. *Opt. Mater.* **2013**, *35*, 322–331. [CrossRef]
40. Kowalski, R.M.; Komar, J.; Solarz, P. On the combination of praseodymium and cerium, a new concept of improving orange-red luminescence. *J. Alloys Compd.* **2020**, *848*, 156228. [CrossRef]
41. Blagden, N.; Davey, R.J. Polymorph selection: Challenges for the future? *Cryst. Growth Des.* **2003**, *3*, 873–885. [CrossRef]
42. Meundaeng, N.; Rujiwatra, A.; Prior, T.J. Polymorphism in metal complexes of thiazole-4-carboxylic acid. *Transit. Met. Chem.* **2016**, *41*, 783–793. [CrossRef]
43. Shannon, R.D. Revised effective ionic radii and systematic studies of interatomic distances in halides and chalcogenides. *Acta Crystallogr. Sect. A* **1976**, *32*, 751–767. [CrossRef]
44. Eyring, L. The binary rare earth oxides. In *Handbook on the Physics and Chemistry of Rare Earths*; Gschneidner, K.A., Jr., Eyring, L., Eds.; Elsevier BV: Amsterdam, The Netherlands, 1979; Volume 3, pp. 337–399.
45. Kumar, R.; Singh, U.P. Molecular structure, photophysical and thermal properties of samarium(III) complexes. *J. Mol. Struct.* **2008**, *875*, 427–434. [CrossRef]

46. Mazurek, J.; Lisowski, J. Chiral macrocyclic lanthanide complexes derived from (1*R*, 2*R*)-1, 2-diphenylethylenediamine and 2,6-diformylpyridine. *Polyhedron* **2003**, *22*, 2877–2883. [CrossRef]
47. Matthes, P.R.; Nitsch, J.; Kuzmanoski, A.; Feldmann, C.; Steffen, A.; Marder, T.B.; Müller-Buschbaum, K. The series of rare earth complexes [Ln_2Cl_6(μ-4,4′-bipy)$(py)_6$], Ln=Y, Pr, Nd, Sm-Yb: A molecular model system for luminescence properties in MOFs based on $LnCl_3$ and 4,4′-bipyridine. *Chem. Eur. J.* **2013**, *19*, 17369–17378. [CrossRef] [PubMed]
48. Lewis, D.J.; Moretta, F.; Holloway, A.T.; Pikramenou, Z. Evaluation of quinoline as a remote sensitiser for red and near-infrared emissive lanthanide(III) ions in solution and the solid state. *Dalton Trans.* **2012**, *41*, 13138–13146. [CrossRef] [PubMed]
49. Mahato, M.; Jana, P.P.; Harms, K.; Nayek, H.P. Lanthanide(III) morpholine 4-dithiocarbamate complexes: Pr(III) derivative shows first example of polymeric lanthanide(III) dithiocarbamate. *RSC Adv.* **2015**, *5*, 62167–62172. [CrossRef]
50. Chow, C.Y.; Eliseeva, S.V.; Trivedi, E.R.; Nguyen, T.N.; Kampf, J.W.; Petoud, S.; Pecoraro, V.L. Ga^{3+}/Ln^{3+} metallacrowns: A promising family of highly luminescent lanthanide complexes that covers visible and near-infrared domains. *J. Am. Chem. Soc.* **2016**, *138*, 5100–5109. [CrossRef]
51. Satheesh Chandran, P.R.; Soumya Mol, U.S.; Drisya, R.; Sudarsanakumar, M.R.; Prathapachandra Kurup, M.R. Structural studies of poly [(μ_2-acetato)(μ_3-5-aminoisophthalato) diaquacerium(III) monohydrate]: A new three dimensional fluorescent metal-organic framework constructed from dimers of CeO_9 polyhedra with hydrophilic 'S' shaped channels. *J. Mol. Struct.* **2017**, *1137*, 396–402. [CrossRef]
52. Zhou, X.; Wang, H.; Jiang, S.; Xiang, G.; Tang, X.; Luo, X.; Li, L.; Zhou, X. Multifunctional luminescent material Eu(III) and Tb(III) complexes with pyridine-3,5-dicarboxylic acid linker: Cystal structures, tunable emission, energy transfer, and temperature sensing. *Inorg. Chem.* **2019**, *58*, 3780–3788. [CrossRef]
53. Hasegawa, M.; Ohtsu, H.; Kodama, D.; Kasai, T.; Sakurai, S.; Ishii, A.; Suzuki, K. Luminescence behaviour in acetonitrile and in the solid state of a series of lanthanide complexes with a single helical ligand. *New J. Chem.* **2014**, *38*, 1225–1234. [CrossRef]
54. Seidel, C.; Lorbeer, C.; Cybińska, J.; Mudring, A.-V.; Ruschewitz, U. Lanthanide coordination polymers with tetrafluoroterephthalate as a bridging ligand: Thermal and optical properties. *Inorg. Chem.* **2012**, *51*, 4679–4688. [CrossRef]
55. Wang, J.-J.; Liu, C.-S.; Hu, T.-L.; Chang, Z.; Li, C.-Y.; Yan, L.-F.; Chen, P.-Q.; Bu, X.-H.; Wu, Q.; Zhao, L.-J.; et al. Zinc(II) coordination architectures with two bulky anthracene-based carboxylic ligands: Crystal structures and luminescent properties. *CrystEngComm* **2008**, *10*, 681–692. [CrossRef]
56. Liu, C.S.; Shi, X.S.; Li, J.R.; Wang, J.J.; Bu, X.H. Cd(II) coordination architectures with mixed ligands of 3-(2-pyridyl)pyrazole and pendant carboxylate ligands bearing different aromatic skeletons: Syntheses, crystal structures, and emission properties. *Cryst. Growth Des.* **2006**, *6*, 656–663. [CrossRef]
57. Carnall, W.T.; Fields, P.R.; Rajnak, K. Electronic energy levels in the trivalent lanthanide aquo Ions. I. Pr^{3+}, Nd^{3+}, Pm^{3+}, Sm^{3+}, Dy^{3+}, Ho^{3+}, Er^{3+}, and Tm^{3+}. *J. Chem. Phys.* **1968**, *49*, 4424–4442. [CrossRef]
58. Carnall, W.T.; Fields, P.R.; Rajnak, K. Electronic energy levels of the trivalent lanthanide aquo ions. IV. Eu^{3+}. *J. Chem. Phys.* **1968**, *49*, 4450–4455. [CrossRef]
59. Carnall, W.T.; Fields, P.R.; Rajnak, K. Electronic energy levels of the trivalent lanthanide aquo ions. III. Tb^{3+}. *J. Chem. Phys.* **1968**, *49*, 4447–4449. [CrossRef]
60. Huskowska, E.; Turowska-Tyrk, I.; Legendziewicz, J.; Riehl, J.P. The structure and spectroscopy of lanthanide(III) complexes with 2, 2′-bipyridine-1,1′-dioxide in solution and in the solid state: Effects of ionic size and solvent on photophysics, ligand structure and coordination. *New J. Chem.* **2002**, *26*, 1461–1467. [CrossRef]
61. Chawla, S.; Roy, T.; Majumder, K.; Yadav, A. Red enhanced YAG: Ce, Pr nanophosphor for white LEDs. *J. Exp. Nanosci.* **2014**, *9*, 776–784. [CrossRef]
62. Wang, Y.; Ding, J.; Zhao, Z.; Wang, Y. A cerium doped scandate broad orange-red emission phosphor and its energy transfer-dependent concentration and thermal quenching character. *Inorg. Chem.* **2018**, *57*, 14542–14553. [CrossRef]
63. Hasegawa, T.; Kim, S.W.; Ueda, T.; Ishigaki, T.; Uematsu, K.; Takaba, H.; Toda, K.; Sato, M. Unusual, broad red emission of novel Ce^{3+}-activated $Sr_3Sc_4O_9$ phosphors under visible-light excitation. *J. Mater. Chem. C* **2017**, *5*, 9472–9478. [CrossRef]
64. Aquino, L.E.D.N.; Barbosa, G.A.; Ramos, J.D.L.; Giese, S.O.K.; Santana, F.S.; Hughes, D.L.; Nunes, G.G.; Fu, L.; Fang, M.; Poneti, G.; et al. Seven-coordinate Tb^{3+} complexes with 90% quantum Yields: High-performance examples of combined singlet- and triplet-to-Tb^{3+} energy-transfer pathways. *Inorg. Chem.* **2021**, *60*, 892–907. [CrossRef] [PubMed]
65. Binnemans, K. Interpretation of europium(III) spectra. *Coord. Chem. Rev.* **2015**, *295*, 1–45. [CrossRef]
66. Binnemans, K. Lanthanide-based luminescent hybrid materials. *Chem. Rev.* **2009**, *109*, 4283–4374. [CrossRef]
67. Martin, A.; Narayanaswamy, R. Studies on quenching of fluorescence of reagents in aqueous solution leading to an optical chloride-ion sensor. *Sens. Actuators B Chem.* **1997**, *39*, 330–333. [CrossRef]
68. Rycerz, L.; Gaune-Escard, M. Thermodynamics of $EuCl_3$: Experimental enthalpy of fusion and heat capacity and estimation of thermodynamic functions up to 1300 K. *Z. Naturforschung A* **2002**, *57*, 215–220. [CrossRef]
69. Rycerz, L.; Gaune-Escard, M. Enthalpies of phase transitions and heat capacity of $TbCl_3$ and compounds formed in $TbCl_3$–MCl systems (M= K, Rb, Cs). *J. Therm. Anal. Calorim.* **2002**, *68*, 973–981. [CrossRef]
70. Amoroso, A.J.; Thompson, A.M.C.; Jeffery, J.C.; Jones, P.L.; McCleverty, J.A.; Ward, M.D. Synthesis of the new tripodal ligand tris-[3-(2′-pyridyl)pyrazol-1- yl]hydroborate, and the crystal structure of its europium(III) complex. *J. Chem. Soc. Chem. Commun.* **1994**, 2751–2752. [CrossRef]

71. Salinas Uber, J.; Vogels, Y.; van den Helder, D.; Mutikainen, I.; Turpeinen, U.; Fu, W.T.; Roubeau, O.; Gamez, P.; Reedijk, J. Pyrazole-based ligands for the [copper–TEMPO]-mediated oxidation of benzyl alcohol to benzaldehyde and structures of the Cu coordination compounds. *Eur. J. Inorg. Chem.* **2007**, *2007*, 4197–4206. [CrossRef]
72. Sheldrick, G.M. SHELXT—Integrated space-group and crystal-structure determination. *Acta Crystallogr. Sect. A Found. Adv.* **2015**, *71*, 3–8. [CrossRef]
73. Sheldrick, G.M. Crystal structure refinement with SHELXL. *Acta Crystallogr. Sect. C Struct. Chem.* **2015**, *71*, 3–8. [CrossRef]
74. Pennington, W.T. DIAMOND—Visual crystal structure information system. *J. Appl. Crystallogr.* **1999**, *32*, 1028–1029. [CrossRef]
75. Macrae, C.F.; Sovago, I.; Cottrell, S.J.; Galek, P.T.; McCabe, P.; Pidcock, E.; Platings, M.; Shields, G.P.; Stevens, J.S.; Towler, M. Mercury 4.0: From visualization to analysis, design and prediction. *J. Appl. Crystallogr.* **2020**, *53*, 226–235. [CrossRef] [PubMed]
76. Coelho, A.A. TOPAS and TOPAS-Academic: An optimization program integrating computer algebra and crystallographic objects written in C++: An. *J. Appl. Crystallogr.* **2018**, *51*, 210–218. [CrossRef]
77. Wrighton, M.S.; Ginley, D.S.; Morse, D.L. Technique for the determination of absolute emission quantum yields of powdered samples. *J. Phys. Chem.* **1974**, *78*, 2229–2233. [CrossRef]